3. International Conference on New Research and Development in Technical and Natural Science,

ICNRDTNS

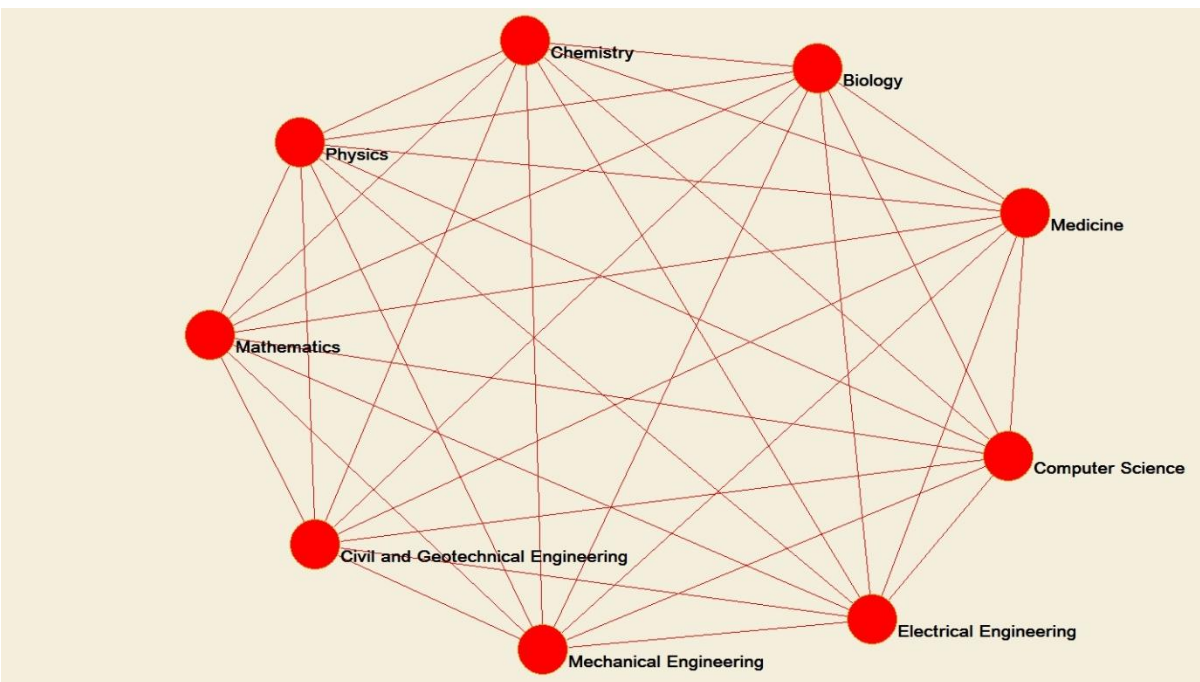

Slovenia, 20. December 2022

The organizers of the 3. International Conference on New Research and Development in Technology and Natural Sciences ICNRDTNS, dear participants and guests, are grateful for your contributions at another traditional meeting of all those interested in the use of mathematics, physics, chemistry, biology, medicine, computer science, electrical engineering, mechanical engineering , construction and geotechnics and all related high technologies in the fields of engineering and science. Presentation be only online.

Assist. Prof. Dr. Matej Babič, Ph.D.

International Program Committee General Chair

Organized by Complex System Company s.p.

Editor: Assist. Prof. Dr. Matej Babič

Publisher: Complex System Company s.p., Podgradje

Circulation: Elektronic edition

Date: december, 2022

icnrdtns.net

Kataložni zapis o publikaciji (CIP) pripravili v Narodni in univerzitetni knjižnici v Ljubljani

COBISS.SI-ID 137890051

ISBN 978-961-07-1446-0 (PDF)

<u>International Organizing Committee</u>

Assist. Prof. Dr. Matej Babič, **President,** Faculty of Information Studies in Novo Mesto, Slovenia
Prof. Dr. Gyula Varga, University of Miskolc, Hungary
Prof. Dr. Cristiano Fragassa, University of Bologna, Italy
Prof. Dr. Dragan Marinković, TU Berlin, Germany
Prof. Dr. Michele Calì, University of Catania, Italy

<u>International Scientific Committee</u>

Prof. Dr. Borislav Savkovic, University of Novi Sad, Serbia
Prof. Dr. Branko Mativić, Vinča Institute, Beograd, Serbia
Dr. Kumar Dookhitram, University of Technology, Mauritius
Prof. Dr. Bojan Đurin, University of North, Varaždin, Croatia
Prof. Dr. Maja Ruzic Baf, University Juraj Dobrila of Pula, Croatia
Prof. Dr. Karolj Skala, Ruđer Bošković Institute, Zagreb, Croatia
Prof. Dr. Daniel Ghiculescu, Polyethnic University of Bucharest, Romania
Dr. George Seritan, Polytechnic University of Bucharest, Romania
Prof. Dr. Grzegorz Lesiuk, Wrocław University, Poland
Dr. Michał Jakubowicz, Poznan University of Technology
Dr. Abdulhamit Subasi, University of Turku, Finland
Dr. Emilio Ramírez Juidías, University of Sevillie, Spain
Prof. Dr. Rita Ambu, University of Cagliari, Cagliari, Italy
Dr. Mirosław Rucki, University of Technology and Humanities in Radom, Poland

Programm

Assessment of 3D digital models of *Madygenerpeton pustulatum* holotype

Yaroslav Garashchenko[1], Ilja Kogan[2], Mirosław Rucki[3)*], Edwin Gevorkian[3]

1) National Technical University, Kharkiv Polytechnic Institute, Department of Integrated Technologies of Mechanical Engineering, Ukraine
2) TU Bergakademie Freiberg, Geological Institute, Germany
3) Faculty of Mechanical Engineering, Kazimierz Pulaski University of Technology and Humanities in Radom, Poland
*Corresponding author: m.rucki@uthrad.pl

The range of possibilities for investigating, visualizing and replicating unique fossils has greatly widened due to the development of digital methods of surface and tomographic 3D scanning, virtual representation and 3D printing over the past two decades. This opens up a nearly unlimited field of applications including the creation of photorealistic 3D models that can be used for teaching and virtual exhibits, remote collaboration on specimens, anatomical studies, digital restoration, functional modelling or fabrication of analogue copies. At the same time, digital methods of investigation and reproduction involve only little contact and are genuinely non-destructive, which means that the risk of damaging the precious specimens is reduced to unlikely accidents during transport and manipulation while digitizing them.

Despite the increasing use of digital techniques, only few comparative studies have attempted to assess fidelity of digitized or printed models obtained by various approaches and devices. Surprisingly little has been done especially on comparing models derived from computed tomography, which is a method designed to represent volumes, with models produced using the more accessible surface-based digitization methods.

To fill in this gap, we are performing comparative analyses of digital and printed models of a complex fossil specimen on the example of the holotype of *Madygenerpeton pustulatum*, a 'reptiliomorph amphibian' from the mid-Triassic fossil locality Madygen in Kyrgyzstan, Central Asia. The Madygen Formation has yielded a wealth of diverse and well-preserved remains of aquatic and terrestrial plants, invertebrates, vertebrates and trace fossils, giving an unparalleled insight into a 237 million years old continental ecosystem of the Northern hemisphere. This record justifies Madygen's status as one of world's most significant fossil lagerstätten of the Mesozoic, making it the center of a potential UNESCO global geopark. A late-surviving member of the predominantly Permian Chroniosuchia, *Madygenerpeton* is known from fragments of the dorsal carapace belonging to at least three individuals and one detached and slightly deformed skull lacking the lower jaw, which constitutes the holotype of the taxon. Skull roofing bones are covered by minute tubercles, which make both mechanical preparation and traditional replication using casts especially delicate. Furthermore, structures from the underside of the specimen and parts of the dentition are still covered by sediment, which cannot be removed without exposing the fossil to a high risk of breakage. Computed microtomography (μCT) offers a solution to this challenge, giving the possibility to differentiate between bone and sediment manually or, when the density contrast is sufficient, even automatically. However, for the sake of comparative analysis, the whole-surface model obtained from μCT scanning is needed. It has been produced by a custom-built YXLON μCT scanner at the Museum für Naturkunde Berlin and compared with several surface models obtained from different 3D scanning devices.

An outstanding feature of μCT scanning is its ability to build a 3D model of *Madygenerpeton* skull free of the sedimentary additions, unable to be removed mechanically. Obviously, such a small, irregular details revealed by tomography and seen in Figure 1a, couldn't be extracted undamaged from the fossil. On the other hand, the analysis of the distances between the scanned surfaces from different devices showed that the tomography (point #8) provided the most distanced model from the reference one obtained with AR Strato.

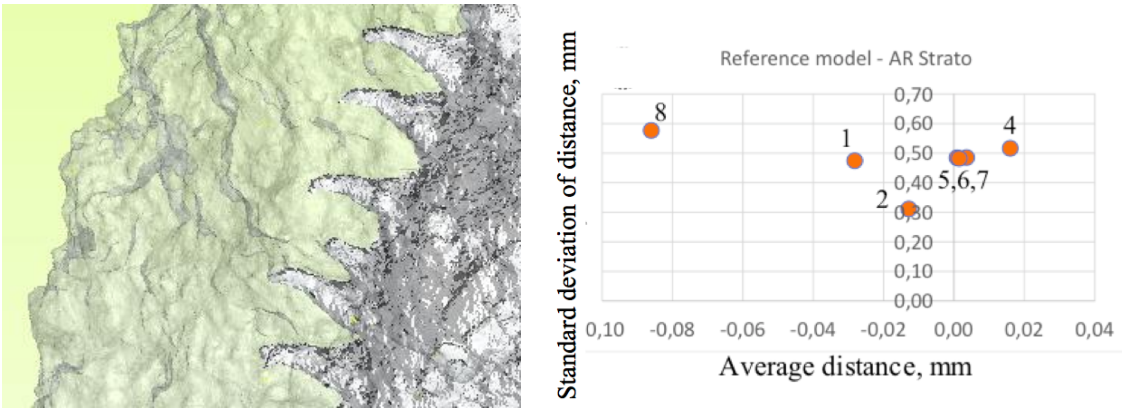

Fig. 1. Analysis of the μCT model: a) details of the skull hidden in sedimentary rock, b) distances between 3D surfaces obtained from different scanners (1 – AICON; 2 – AR Crysta; 3 – AR Strato; 4 – ARTEC; 5 – CREAFORM GoScan; 6 – CREAFORM HandyScan; 7 – EinScan Pro; 8 – Yxlon μCT)

The distances from μCT model were the largest for each reference. Apart from that, the calculated volume of μCT model was the smallest, while its surface was one of the largest. Moreover, it had the largest number of polygons. This demonstrates that μCT model represents the *Madygenerpeton* skull in a much more detailed way.

Comparative analysis of two models – one included the sedimentary rocks, and the other excluded them – enabled the assessment of the dimensions of the unwanted additions. Statistically, thickness of sediments t_s can be described by maximal value $\{t_s\}_{max}$ = 8.2 mm, statistical mean $\bar{t}_s = 0.69$ mm, and square root deviation $\square\{t_s\}$ = 1.18 mm. Since the models had different geometry and differed from one another in respect of the number of triangles, statistical parameters appeared to be different depending on which of the two models was tested, and which one was used as a reference. Table 1 shows the results of comparative analysis of two models in terms of distance between the respective triangles.

Table 1. Results of initial statistical analysis of the distances between two 3D models

Reference model	Test model	Distance statistics					
		maximum		average $\overline{\Delta_d}$			standard deviation $\sigma\{\Delta_d\}$
		positive	negative	all	positive	negative	
AR Strato	YXLON μCT	2.000	-2.000	-0.0860	0.2664	-0.3006	0.5762
YXLON μCT	AR Strato	1.9899	-1.9981	0.0210	0.0772	-0.0676	0.1191

Comparative analysis of the statistical parameters revealed that μCT model differed the most from all other ones, showing the largest $\overline{\Delta_d}$ and $\sigma\{\Delta_d\}$. It can be explained from the perspective of the radical differences between the scanning principles. The average distance, however, is below 0.12 mm with standard deviation below 0.6 mm. Since these values are close to the accuracy of 3D printing technologies, it is possible to use the MCT model for further additive manufacturing of the *Madygenerpeton pustulatum* skull.

Acknowledgement: The paper was prepared thanks to Erasmus+ mobility.

Mechanical Performance of Structural Rebars subjected to several Mechanical tests

Authors: <u>Kayode Olaleye</u>[1], Zielonka Pawel[1], Duda Szymon[1], Cristine Caroline Campos Lopes[2], Bruno Pedrosa[3], Lesiuk Grzegorz[1], Katarzyna Żołyńska[1], Wojciech Błażejewski[1]

1 Wroclaw University of Science and Technology, Wroclaw, Poland

2 Federal University of Minas Gerais, Belo Horizonte, Brazil

3 University of Coimbra, Coimbra, Portugal

Abstract

Due to their numerous benefits, such as their high tensile and fatigue strengths, high corrosion resistance, light weight, ease of handling, thermal and electrical insulating properties, and insensitivity to magnetic fields, fiber-reinforced polymer (FRP) bars have been used more and more in the field of structural engineering [1,2,3]. FRP reinforcing bars, on the other hand, have several significant drawbacks, such as creep failure, limited commercial availability, high production costs, anisotropic material properties, limited ductility, low elastic modulus, intolerance to bending (for use as stirrups), and low transverse and lateral strength values in comparison to longitudinal tensile strength [4,5,6]. Another restriction on the usage of FRP bars for structural purposes is the absence or constrained scope of the restrictions in the existing FRP reinforced concrete (RC) norms and regulations. Researchers are working to come up with solutions to the problems associated with the structural usage of FRP bars and are pushing its use as concrete reinforcement due to the multiple positive effects of FRP bars on the service life of structures, the national economy, and the environment. The mutual adhesion, surface friction, and shear interlock bond mechanisms of FRP bars in concrete are comparable to those of steel bars. However, compared to steel bars, FRP bars have entirely different mechanical properties [7,8]. As a result, the evaluation of the flexural behavior of FRP RC members cannot be based on the flexural behavior of RC members with steel reinforcement. Due to the above pros and cons, this research will investigate the mechanical characteristic our homemade composite rebars and they could be utilized as reinforcing phase in concrete and soil.

Acknowledgements:

The research was financed by the National Center for Research and Development of Poland (NCBiR) grant number LIDER/40/0219/L-10/18/NCBR/2019.

References

1. Tomasz, M., Szymon, D., Bartosz, B., Joanna, W., Paweł, Z., & Grzegorz, L. (2022). Flexural and compressive residual strength of composite bars subjected to harsh environments. Engineering Failure Analysis, 133, 105958.
2. Barcikowski, M., Lesiuk, G., Czechowski, K., & Duda, S. (2021). Static and flexural fatigue behavior of GFRP pultruded rebars. Materials, 14(2), 297.
3. Nanni, A., De Luca, A., & Zadeh, H. (2014). Reinforced concrete with FRP bars. Mechanics and design, international standard book no-13, 978-0.
4. GangaRao, H. V., Taly, N., & Vijay, P. V. (2006). Reinforced concrete design with FRP composites. CRC press.
5. ACI Committee. (2015). Guide for the design and construction of structural concrete reinforced with fiber-reinforced polymer (FRP) bars (ACI 440. 1R-15). Farmington Hills, Michigan: American Concrete Institute.
6. Mufti, A. A., & Neale, K. W. (2007). State-of-the-art of FRP and SHM applications in bridge structures in Canada. Proc., Composites & Polycon 2007.
7. FIB (Fédération Internationale du Béton). (2000). Bond of reinforcement in concrete. FIB Bulletin 10.
8. Bond, A. C. I. (2003). Development of Straight Reinforcing Bars in Tension. ACI 408R-03.

Analysis of the Deceleration Methods of Fatigue Crack Growth Rates under Mode I Loading Type in Pearlitic Rail Steel

Authors: Szymon Dziuba[1], Kayode Olaleye[1], Bruno Pedrosa[3], Lesiuk Grzegorz[1], Jose A.F.O. Correia[3], Abilio M.P. De Jesus[3], H. Nykyforchyn[4], Olha Zvirko[4]

1 Wroclaw University of Science and Technology, Wroclaw, Poland

2 University of Coimbra, Coimbra, Portugal

3 University of Porto, Porto, Portugal

4 Karpenko Physico-Mechanical Institute of the NAS, Lviv, Ukraine

The main goal of this paper is to compare different (physically) approaches in crack growth rate deceleration in pearlitic steel commonly used for rail manufacturing [1]. The paper presents a comparison of fatigue crack growth rates from raw rail steel with steel reinforced with composite patches, the implementation of the stop-hole technique, and the application of an "anti-crack growth fluid". All these methods are widely used as deceleration methods of fatigue crack growth. Carbon fiber-reinforced polymer (CFRP) patches are still of particular interest in various applications in civil engineering [2-5]. The fatigue crack growth process is strongly associated with the crack driving force and its local condition. In [6-8], authors explained crack growth rate decreasing with an effective stress intensity factor (crack closure concept [9]) based on ΔK_{eff} concept. This assumption allows us to explain, simply using a closure parameter, the role of crack closure in analytical formulas. Recently, the concept of crack closure triggering due to the application of fluid [10] into the crack was successfully validated for low-carbon steel [6].

The material from which all the samples presented in the study were prepared was taken from the rail that had previously been withdrawn from use, and its profile conformed to UIC60 [11]. In addition to the samples made from the base material, samples were also reinforced with a carbon fiber material. CFRP polymer is an extremely strong and light fiber-reinforced plastic. The tests were carried out on five types of samples, which are listed below:

- raw steel material,
- raw steel material with stop-hole technique,
- raw steel material with a wide CFRP patch (full face),
- raw steel material with a narrow CFRP patch (strip),
- raw steel material with the "anti-crack growth fluid" [10].

For the experimental campaign, compact tension (CT) specimens were prepared in accordance with ASTM E647 [12] standard. All specimens were tested using constant load amplitude methods with a maximum loading F_{max} = 8 kN and stress ratio $R = \sigma_{min}/\sigma_{max} = 0.1$ to analyse the efficiency of different strategies of fatigue crack growth rate deceleration.

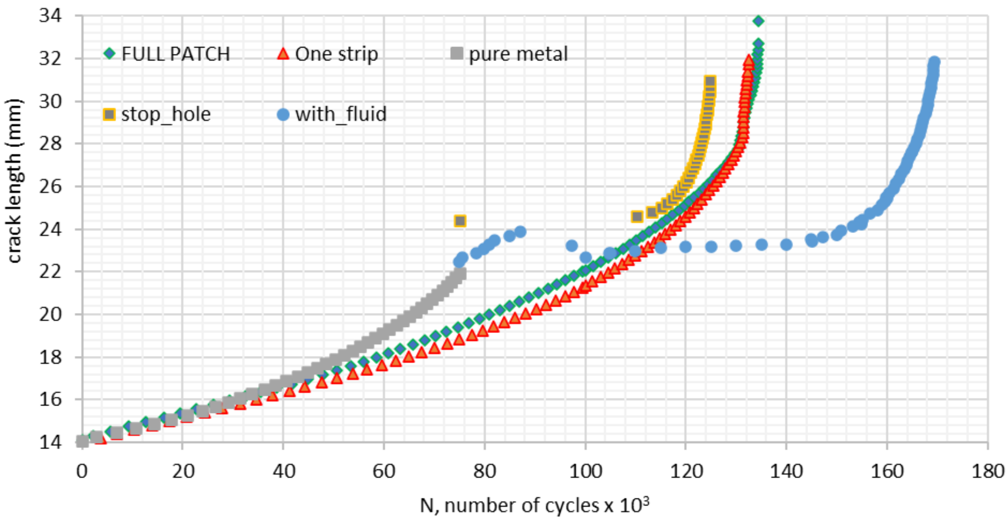

Figure 1. Fatigue crack growth curves for all tested specimens

Results had shown that the fastes fatigue crack grow is obtained with the raw material and the slowest is obtained when the "anti-crack growth fluid" is applied. Additionally, the study on fatigue fracture surfaces using light and scanning electron (SEM) microscopy to analyse the crack growth mechanism was carried out. As a result of fluid activity, fatigue crack closure occurred leading to a significant decrease in the crack driving force which resulted in lower fatigue crack growth. Figure 1 presents fatigue lifetime curves for all specimens tested in the same loading conditions. As it is noticeable, comparable effect is obtained for the designed stop hole technique and composite CFRP patches. Similar frack growth was found using one strip or full patch of CFRP which is in accordance with the results presented in Lesiuk *et al*. [13]. Authors implemented a numerical analysis focus on the CFRP effect on the stress intensity factor showing the same reduction level when using a strip or a full patch CFRP. For direct comparison of the fluid activation effect on the crack deceleration for metallic specimens (without CFRP) kinetic fatigue fracture diagram (KFFD) was constructed, as shown in Figure 2.

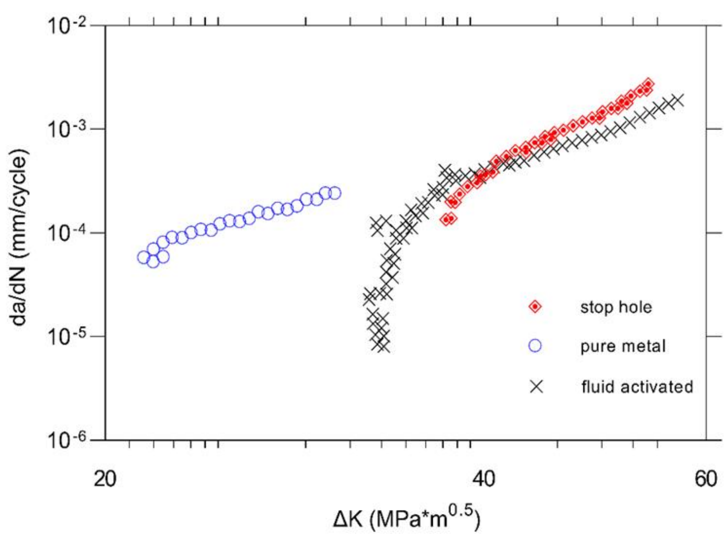

Figure 2. Comparison of fatigue crack growth rates for pure metallic specimens (stop hole, CT specimen with injected fluid).

Keywords: pearlitic steel; CFRP patches; crack retardation; fatigue crack growth; failure analysis

References

1. Lesiuk, G.; Smolnicki, M.; Mech, R.; Ziety, A.; Fragassa, C. Analysis of fatigue crack growth under mixed mode (I+ II) loading conditions in rail steel using CTS specimen. Eng. Fail. Anal. 2020, 109, 104354.
2. Lesiuk, G.; Katkowski, M.; Correia, J.; de Jesus, A.M.; Blazejewski, W. Fatigue crack growth rate in CFRP reinforced constructional old steel. Int. J. Struct. Integr. 2018, 9, 381–395.
3. Yu, Q.Q.; Wu, Y.F. Fatigue retrofitting of cracked steel beams with CFRP laminates. Compos. Struct. 2018, 192, 232–244.
4. Emdad, R.; Al-Mahaidi, R. Effect of prestressed CFRP patches on crack growth of centre-notched steel plates. Compos. Struct. 2015, 123, 109–122.
5. Hosseini, A.; Ghafoori, E.; Motavalli, M.; Nussbaumer, A.; Zhao, X.L. Mode I fatigue crack arrest in tensile steel members using prestressed CFRP plates. Compos. Struct. 2017, 178, 119–134.
6. Khaburskyi, Y.; Slobodyan, Z.; Hredil, M.; Nykyforchyn, H. Effective method for fatigue crack arrest in structural steels based on artificial creation of crack closure effect. Int. J. Fatigue 2019, 127, 217–221.
7. Borrego, L.P.; Ferreira, J.M.; Da Cruz, J.P.; Costa, J.M. Evaluation of overload effects on fatigue crack growth and closure. Eng. Fract. Mech. 2003, 70, 1379–1397. Metals 2021, 11, 584 13 of 13
8. Maierhofer, J.; Simunek, D.; Gänser, H.P.; Pippan, R. Oxide induced crack closure in the near threshold regime: The effect of oxide debris release. Int. J. Fatigue 2018, 117, 21–26.
9. Elber, W. Fatigue crack closure under cyclic tension. Eng. Fract. Mech. 1970, 2, 37–45
10. Nykyforchyn, H.; Pustovyi, V.; Slobodyan, Z.; Khaburskyi, Y.; Barna, R.; Zvirko, O.; Kret, N. The Method of Fatigue Crack Growth Arrest. Patent of Ukraine No.128514, 15 September 2018. (In Ukrainian).
11. Lesiuk, G.; Smolnicki, M.; Mech, R.; Ziety, A.; Fragassa, C. Analysis of fatigue crack growth under mixed mode (I+ II) loading conditions in rail steel using CTS specimen. Eng. Fail. Anal. 2020, 109, 104354.
12. Lesiuk, G.; Pedrosa, B.A.; Ziety, A.; Błazejewski, W.; Correia, J.A.; De Jesus, A.M.; Fragassa, C. Minimal invasive diagnostic ˙ capabilities and effectiveness of CFRP-Patches repairs in long-term operated metals. Metals 2020, 10, 984.
13. Lesiuk, G.; Pedrosa, B.A.; Ziety, A.; Błazejewski, W.; Correia, J.A.; De Jesus, A.M.; Fragassa, C. Minimal invasive diagnostic ˙ capabilities and effectiveness of CFRP-Patches repairs in long-term operated metals. Metals 2020, 10, 984.

A graphical approach based on slipping to evaluate necking phenomena during tensile stress

Michele Calì, Mario Grasso

Electric, Electronics and Computer Engineering Department, University of Catania, Catania, Italy, michele.cali@unict.it

What are the characteristics in the tensile test that determine the shrinkage and collapse in the centerline? The experimental results reported in the book 'Construction Science, Vol. 2, p. 370, Fig. 264', by S. Timoshenko', show that for a tensile rod, a passing limiting force can be evaluated (Figs. 1/a, 1/b) between: negligible elongations of the specimen, at the beginning highly sensitive elongations, and that by analogy to the instability limiting force for compressive load (peak load), is referred to here as 'F lim traction limit force'.

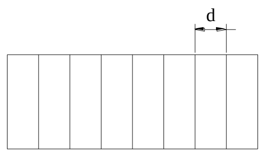

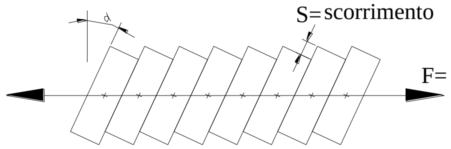

Instability is characterized by rotation and subsequent slipping. In the graph Fig. 2/c, the pressure over time is reported in different sections (centerline, extremities and intermediate sections), where the following aspects are highlighted:

- Section 2 of the centreline is subject to pressure $\boldsymbol{2\frac{F}{A}}$, and also passes from the value P=0 to the value $\boldsymbol{P = 2\frac{F}{A}}$ suddenly.
- Section 3 is subject to a maximum pressure $\boldsymbol{P = 2\frac{F}{A}}$ like section 2, but changes from p=0 to maximum value $\boldsymbol{P = 2\frac{F}{A}}$ gradually;
- Sections 4 and 5, are subject to a maximum pressure $\boldsymbol{P = \frac{F}{A}}$. Ultimately, section 2, in addition to reaching a pressure double that of extreme section 6, goes from zero pressure to this maximum value instantaneously, circumstances that make it more vulnerable. We can also say that on average the pressure along the rod passes from the value$\boldsymbol{P_{estremit\grave{a}} = \frac{F}{A}}$ at the end, at the value $\boldsymbol{P_{mezzeria} = 2\frac{F}{A}}$ in the centerline. A free rod without constraints and subject to impulsive forces at the ends.

Some cases related to different patterns of applied forces are reported. With reference to Fig. 2, we have: F = Applied impulsive force; ta = to/4 = Duration of application force; to = Rod time length. Fig. 2 shows: a) the following frames highlighting the position of the pressure waves oscillating back and forth along the rod; (b) how the initial rod with free ends and on which the 'F' forces act, is equivalent to a rod of length 'to/2' and embedded in the corresponding centreline; c) the pressure in some sections over time. Pressure that varies cyclically with period T = 2To.

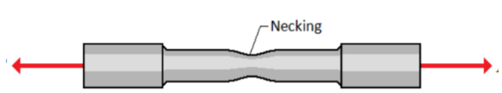

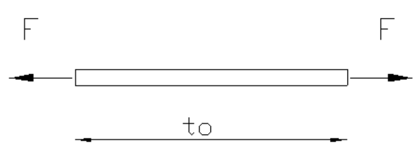

Analyzing the pressure diagrams c), the following considerations can be made: 1) the impulse poured by external forces on the structure, is worth: $\boldsymbol{I_e = 2 \cdot (F \cdot \frac{t_o}{4}) = F \cdot \frac{t_o}{2}}$; 2) the area enclosed in each pressure range, is $\boldsymbol{I = F \cdot \frac{t_o}{2} = I_e}$;

3) In the '2' centerline section, this pulse acts in a time interval $\boldsymbol{\Delta t} = \frac{t_o}{4}$, while in the other sections in a longer time and with the maximum pressure that tends to decrease from section '4' onwards;
4) In section '5', the impulse $\boldsymbol{I} = \boldsymbol{F}\frac{t_o}{2}$ It is divided into two parts: $\boldsymbol{F}\frac{t_o}{4} + \boldsymbol{F}\frac{t_o}{4}$, with a maximum pressure equal to half of what is in the centerline;

5) In the end section '6', there is a pulse equal to half of what is in the centerline, as well as only at the beginning of the impact.
6) in section '6', the pressure is F/A only during the application of the external force, the boundary condition being met: [pressure = 0 for 't' over to/4]
From all of the above, it can be deduced that the centerline section is the most critically solicited. This circumstance can be taken as a motivation for why in the tensile test, the tightening and subsequent rupture takes place right in the middle of the specimen. As conseguence of these two results, consider Fig. 3, a rod subject to force

$$\boldsymbol{F_1} = \boldsymbol{F_{lim}} - \Delta \boldsymbol{F_1} \tag{1}$$

at the ends, being:
- $\boldsymbol{F_{lim}}$= tensile instability limiting force;
- $\Delta \boldsymbol{F_1}$= quantity of minimum force for now undefined and in any case just less than the amount of increment generated by the machine during the tensile test;
- $\boldsymbol{F_1}$ applied on the rod for a long time and such that inside the body there are no sliding between molecules, nor stray pressure waves, and that in terms of voltage (1) becomes:

$$\boldsymbol{\sigma_1} = \boldsymbol{\sigma_{lim}} - \Delta \boldsymbol{\sigma_1} \tag{2}$$

where: $\boldsymbol{\sigma_1} = \frac{F_1}{A}$ $\quad \boldsymbol{\sigma_{lim}} = \frac{F_{lim}}{A}$ $\quad \Delta\boldsymbol{\sigma_1} = \frac{\Delta F_1}{A}$

In such circumstances, on each section of the rod there is a tensile stress σ1 constant (Fig. 3).

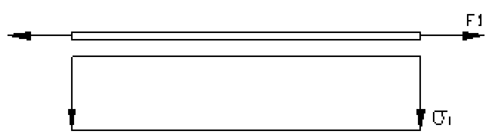

Fig. 3 Tension diagram σ1 for $\boldsymbol{F_1} = \boldsymbol{F_{lim}} - \Delta \boldsymbol{F_1}$.

From this configuration, apply a further impulsive action ΔF2 to the rod. in traction and such that it is

$\Delta \boldsymbol{F_2} < \Delta \boldsymbol{F_1}$ and therefore, considering the (1) $\boldsymbol{F_1} + \Delta \boldsymbol{F_2} = (\boldsymbol{F_{lim}} - \Delta \boldsymbol{F_1}) + \Delta \boldsymbol{F_2} < \boldsymbol{F_{lim}}$ (3)

Δσ2=ΔF2A<(Δσ1=ΔF1A) or from eq. (3) σ1+Δσ2=σlim-Δσ1+Δσ2<σlim (4)

which is: F1+2 ΔF2>Flim or σ1+2 Δσ2>σlim (5)

Considering the previous analysis Fig. 2/c, in which the tensile impulse at both ends generates a tensile stress trend such that on average in the centerline it doubles compared to the ends Fig. 4, we have:

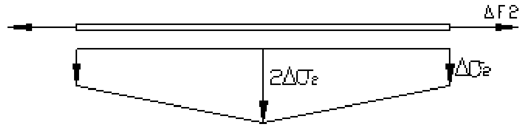

Fig. 4 Average tensile stress diagram along the pulse rod ΔF1.

Summing the effects due to the initial force F1 and those due to ΔF2, that is, adding up the graphs Fig. 3 + Fig. 4, we get Fig5

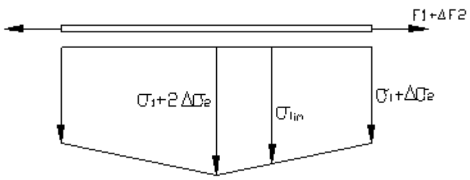

Fig. 4 Average tensile stress diagram along the pulse rod ΔF1.

Summing the effects due to the initial force F1 and those due to ΔF2, that is, adding up the graphs Fig. 3 + Fig. 4, we get Fig5

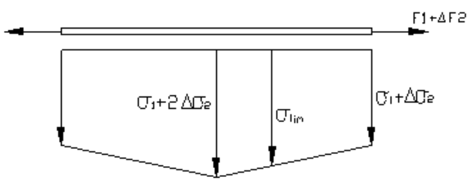

Fig. 5 Total tension tensile diagram rod.

By choosing appropriately the values of F1, ΔF1, ΔF2, we can make sure that it results: $\sigma1+2\ \Delta\sigma2>\sigma lim>\sigma1+\Delta\sigma2$ (6)

Therefore, it turns out that the centerline zone exceeds the tension limit tension of tensile instability and therefore zone of ignition of restriction.σlim

MAPPING OF TOURIST DIVING ATTRACTIONS IN THE ADRIATIC SEA

Vlatka Davidović[1], Viktor Medakov[2], Matej Pogarčić[3]

[1]Polytechnic of Rijeka, Croatia, vlatka.davidovic@veleri.hr

[2]University Juraj Dobrila of Pula, Croatia, viktor.medakov@gmail.com
[3]Vodogradnja d.o.o, Rijeka, Croatia, matej.pogarcic@gmail.com

ABSTRACT

Applied geography in the form of maps and spatial data has served discovery, planning, collaboration and conflict through many years of mankind. Like many other aspects of life, in the last five decades the way we collect and use spatial information has been deeply influenced by modern technology, and GIS software and hardware are the results of these advances. GIS becomes an increasingly important tool in environmental management, marketing, tourism and many other components of our daily lives. The aim of this paper is to show the possibilities that this technology provides us theoretically and through an independent project - mapping and cadaster of sunken ships and other attractions in the Adriatic Sea.

Keywords: GIS, mapping, attractions, Adriatic Sea

1. INTRODUCTION

The term GIS has been attempted to be defined many times and for this reason there is no single concluding definition that we can use. The diversity of these definitions is explained by Pickles [1] by saying that the definition of a GIS system varies depending on who defines GIS and also states that the definition of a GIS is very likely to change with future developments in technology [2]. In general, the definitions of GIS systems cover three main components: GIS is a computer system, it uses spatial data and it performs various analyses over these spatial data.

It can be said that GIS is a tool for creating and using spatial information with added value.

GIS can exist as a generic framework if the specific application is not considered. In that case, any meaningful process/system that requires spatial data and/or its analysis can be applied. As each information system is the basis for the processes of management and decision-making, GIS expands these properties and gives them a new appearance and a new value. Of course, data and information in GIS are of great importance for specific users, because only with the existence of users any G(IS) becomes a reality with concrete goals and a concrete purpose.

2. DATA IN GIS

Data in GIS systems represent a simplified view of the world and simplified view of physical entities in the world. They include information on the spatial position and scope of the object and information on its non-spatial properties. Spatial data defines the location and shape of each spatial object or phenomenon in two or three-dimensional space [3]. Attribute data is used to record non-spatial characteristics of entities.

When it comes to geographic information systems, the purpose of the spatial data model is to enable the display and management of spatially referenced information [3]. Spatial data structures provide the necessary information to the computer so that it can reconstruct the spatial data model into a digital form. Two data models were used in geographic information systems: raster and vector. Raster is one of the oldest and most widely used models. It is most commonly used in writing, analyzing and visualizing data of a continuous nature such as elevations, temperatures or for example electromagnetic radiation [4]. A vector data model uses a set of coordinates and associated attribute data to specify discrete objects. Coordinate groups determine the location and boundaries of discrete objects and, together with attribute data, create vector objects that we use to display real entities [3]. Triangulated irregular network (TIN) is a data model that is most often used to display terrain height, i.e. it has x, y and z spatial values. TIN, as its name suggests, creates a network of irregular triangles. This model uses indexing shapes to connect adjacent points. Each edge of the triangle is connected to two points which are then connect to other edges. These joins continue recursively until the entire network has been created [3].

3. COLLECTION AND VISUALIZATION OF SPATIAL DATA

Collecting spatial data is one of the most time-consuming and financially expensive GIS tasks. There are various sources of geographic data and also a lot of methods by which they can be entered into GIS. The two main methods of data collection are data retrieval and data transfer. It is important to understand the difference between primary (direct measurements) and secondary (taking data from other sources) data retrieval, which also applies to vector and raster data [5] Primary retrieval of geographic data includes direct measurements of objects. Digital data obtained by measurement can be entered directly into the GIS database or stored in a temporary file before entering. The most common method for raster data retrieval is remote sensing. The term remote sensing encompasses the areas of satellite imaging and aero photography. In vector data retrieval, there are two main branches that are divided into field measurements and GPS. Secondary retrieval of geographic data is the process of creating raster and vector files and databases from existing maps, photographs and other documents [5].

Visualization of spatial data is extremely important in understanding their locations, shapes and surfaces and comes from the need to better understand the nature of these data. Visualization can be done through various software systems, programming languages, their libraries and tools. Spatial data visualization uses and combines different layers obtained using different libraries and plugins.

4. PROJECT OF MAPPING TOURIST DIVING ATTRACTIONS IN THE ADRIATIC SEA

The first step in mapping tourist diving attractions in the Adriatic Sea is data collection. These data are structured and prepared for input into GIS. Then follows the visualization of the data, and after the visualization, cartographic expressions, i.e. the final product, are created.

4.1. DATA COLLECTION

The project began with research and data collection for 4 categories of tourist diving attractions in the Adriatic, namely: shipwrecks, aircraft wrecks, reefs and caves. Data was recorded and processed in Microsoft Excel 2010 version 14.0 as part of the Microsof Office Professional Plus 2010 package. To collect data on shipwrecks, a book entitled Wrecks of modern ships in the Adriatic Sea (*Adriatic Wrecks*) was used as the starting point of the research. The author of the book is Danijel Frka, B.Sc., independent underwater researcher, photographer and historian [6]. Additional literature was also used to collect data on shipwrecks and other categories. Book *The underwater story of Istria* has contributed in the research of the area of Istria [7]. The book *Austro-Hungarian destroyers* was used to find information on Austro-Hungarian destroyers [8]. The literature entitled Crash of an Allied Bristol Beaufighter (NT997) near Senj in October 1944 was also used to check and find missing information [9]. Of course, along with books and professional articles, some websites are used, such as:

- https://h2oglobe.com/
- http://www.ronjenjehrvatska.com/hr/home
- https://www.diving-shark.hr/en/
- https://krnica.com/index.php

Shipwreck attributes

A total of 42 shipwrecks were recorded, all from the territory of the Republic of Croatia, and they were described with 17 attributes. The first and main attribute is the ID that is the primary key and identifier in the database. This is followed by attributes indicating the name of the ship and the minimum and maximum depth expressed in the meters on which the wreck is located. The most important attributes, those without which it is not possible to map the locations of wrecks, are latitude and longitude that are expressed in decimal values. These attributes were the most demanding to find because a lot of literature omits the location of the shipwreck. To find the location of each wreck, more detailed and deeper research was needed, and specifically from different sources (Figures 1 and 2). Information about the dates when the ship sank and when it was built and/or launched was also saved. Information about the type of ship was also recorded, for example whether it was a steamship or a motor propulsion, whether it was a cargo or a war cruiser, and of course, an attribute was added to indicate whether the ship was civilian or belonged to the navy. Very interesting attributes are also the flag under which the ship sailed and why it sank. Later it will be shown that the most ships sank from hitting an underwater mine. The literature used for the research provided information about the length and width of the wreck. Data were also added on the area of sinking, which represents the region or the nearest settlement or island where the ship sank, and generally in which part of the Adriatic the ship sank (north, middle or south). At the very end, we can read what is the minimum diving category required to access the wreck (R1, R2 and R3) where R1 indicates the initial and R3 the most experienced category and the visibility score of the wreck of 1-5, where 1 is the worst and 5 is excellent visibility. Of course, some fields in the table will be remain empty because the data for that attribute could not be found or was different from various sources.

	A	B	C	D	E	F	G	H	I
1	ID	Ime	Min_Dubina	Max_Dubina	Geo_Sirina	Geo_Duzina	Potonuo	Izgraden_Porinut	Tip
2	1	Kostrena	29	35	45,13333	14,21833	19.2.1888	1886.	Teretni jedrenjak
3	2	John Gilmore	35	44	44,83476	13,73183			Teretni parobrod
4	3	Lina	25	55	45,10224	14,27876	14.1.1914	14.4.1879.	Teretni parobrod
5	4	TB 26 Flamingo	41	46	44,72077	13,81163	23.8.1914		Torpiljarka
6	5	Cesare Rossarol I	43	49	44,84142	14,00717	16.11.1918.	15.8.1914.	Razarač
7	6	Pelagosa	51	51	44,41292	14,47923	12.2.1918	1898.	Parobrod
8	7	Varese	33	41	44,81288	13,77931	18.1.1915	1871.	Teretni parobrod
9	8	SS Wildfang	40	40	44,71666	13,21666	4.6.1917.	29.8.1906.	Razarač
10	9	Euterpe	70	79	44,60567	14,79241	11.8.1918.	1886.	Teretni parobrod
11	10	Kaiser Franz Josef	28	45	42,40561	18,52667	17.10.1919.	1890.	Krstarica
12	11	Etnea	28	35	44,636	14,23057	8.11.1894.	14.4.1870.	Teretni parobrod
13	12	Vassilios	25	55	43,00458	16,06517	19.3.1939.	1920.	Teretni parobrod
14	13	Teti	10	34	43,05334	16,04083	23.5.1930.	1883.	Teretni parobrod
15	14	Brioni	45	61	43,01453	16,22913	2.2.1930.		Putničko teretni parobrod
16	15	HMS Coriolanus	11	25	45,3274	13,38998	5.5.1945.	20.10.1940.	Minolovac
17	16	Hans Schmidt	35	45	44,918	13,59388	23.1.1943.	1920.	Teretni parobrod
18	17	Medusa	36	38	44,85013	13,80564	30.1.1942.	10.12.1931.	Podmornica
19	18	TA 35 Giuseppe Dezza	22	30	44,97333	13,6856	17.8.1944.	15.12.1915.	Torpiljarka
20	19	TA 36 Stella Polare	45	65	45,13323	14,22764	18.3.1944.	11.7.1943.	Torpiljarka

Figure 1 Shipwreck Dataset Attributes Part 1

	J	K	L	M	N	O	P	Q	R
1	Pripadnost	Zastava	Potonuo_Zbog	Duzina_Broda	Sirina_Broda	Podrucje_Potonuca	Min_Ronilacka_Kategorija	Ocjena_Vidljivosti	Dio_Jadrana
2	Civilni	Austro-Ugarska	Nevrijeme	42,02	9,38	Istra	R2	4	Sjeverni
3	Civilni			50	8	Istra	R3	4	Sjeverni
4	Civilni	Talijanska	Nevrijeme	70	9	Cres	R2	5	Sjeverni
5	Mornarica	Austro-Ugarska	Podvodna mina	39	4,5	Istra	R3	1	Sjeverni
6	Mornarica	Talijanska	Podvodna mina	85	9	Istra	R3	3	Sjeverni
7	Mornarica	Austro-Ugarska	Torpedo	48,73	6,28	Silba	R3	3	Sjeverni
8	Civilni	Talijanska	Podvodna mina	60	9	Istra	R3	3	Sjeverni
9	Mornarica	Austro-Ugarska	Podvodna mina	67,06	6,26	Istra	R3	1	Sjeverni
10	Civilni	Austro-Ugarska	Torpedo	96,54	11,26	Pag	R3	3	Srednji
11	Mornarica	Austro-Ugarska	Nevrijeme	97,8	14,9	Boka Kotorska	R2	3	Juzni
12	Civilni	Talijanska	Nasukavanje	61	8,7	Unije	R2	4	Sjeverni
13	Civilni	Grčka	Nasukavanje	104	15,1	Vis	R2	5	Srednji
14	Civilni	Talijanska	Nevrijeme	72	8	Vis	R1	5	Srednji
15	Civilni	Austro-Ugarska	Nasukavanje	68,36	9,5	Vis	R3	5	Srednji
16	Mornarica	Britanska	Podvodna mina	49,99	8,43	Istra	R1	2	Sjeverni
17	Civilni	Njemačka	Podvodna mina	99	11,5	Istra	R3	2	Sjeverni
18	Mornarica	Talijanska	Torpedo	61,5	5,65	Istra	R3	2	Sjeverni
19	Mornarica	Njemačka	Podvodna mina	73	7,33	Istra	R2	3	Sjeverni
20	Mornarica	Njemačka	Podvodna mina	82,26	8,5	Istra	R3	3	Sjeverni

Figure 2 Shipwreck Dataset Attributes Part 2

Figure 3 The wreck of the steamship Vis, which sank in 1946 near

Cape Mašnjak at the entrance to Plomin Bay [6]

Attributes of aircraft wreckages

In the research is shown that currently only 4 aircraft wreckage has been discovered in the Adriatic Sea, all during the Second World War between 1941 and 1944. They are described with 15 attributes, most of which are the same as for the previous dataset on shipwrecks with minor differences. Differences are categories of wrecks (Figures 4 and 5). Some attributes from the previous dataset were thrown out, such as visibility and the date when the aircraft was built. These data were mostly not available or were contradictory.

	A	B	C	D	E	F	G	H
1	ID	Ime	Min_Dubina	Max_Dubina	Geo_Sirina	Geo_Duzina	Pad	Zastava
2	1	Bristol Beaufighter	22	22	44,99207	14,89623	1944.	Britanska
3	2	Boeing B 17G	65	72	43,01718	16,21783	6.11.1944.	Americka
4	3	B-24 Libertador	39	52	43,03293	16,26483	17.11.1944.	Americka
5	4	Ju 87 Stuka	13	13	43,65478	15,6344	1941.	Njemacka

Figure 4 Attributes of the aircraft wreckage dataset Part 1

I	J	K	L	M	N	O
Tip	Min_Ronilacka_Kategorija	Duljina	Raspon	Podrucje_Pada	Pao_Zbog	Dio_Jadrana
Lovac-bombarder	R2	12,6	17,6	Senj	Protuzračna artiljerija	Sjeverni
Bombarder	R3	22,78	31,62	Vis	Protuzračna artiljerija	Srednji
Bombarder	R3	20,472	33,528	Vis	Protuzračna artiljerija	Srednji
Bombarder	R1	11	13,8	Žirje	Protuzračna artiljerija	Srednji

Figure 5 Attributes of the aircraft wreckage dataset Part 2

Figure 6 The B-17 flying fortress near Vis lies at a depth of 72 meters [6]

Attributes of the reefs

Data were collected on 14 reefs across Croatia that can be visited and described with 12 attributes. Compared to earlier datasets, there were two new attributes added, which did not appear in previous datasets. The attribute of flora and fauna that categorizes the flora and fauna of the reef into three classes: poor, rich and exist. Current attribute is described with current strength in the reef area: weak, medium and strong. The current attribute directly affects the attribute of the minimum diving category. It is not recommended for beginner diver category R1 to access the location with strong current.

Attributes of the caves

It is important to emphasize that the caves that can be visited are also located in the same locations as some reefs in the previous dataset. In this data set, only caves that are not part any of the reefs are recorded. A total of 37 caves were recorded in this project and it can be said that the southern Adriatic is the richest in this category. The attributes of this data set are exactly the same as the set for reefs.

After collecting and entering the data into the tables, it is necessary to convert the data into a CSV (*Comma separated values*) file so that the data from the table can be entered into the QGIS project. A single .csv file is imported into the project as a layer.

4.2 CREATING A MAP OF THE ADRIATIC SEA

For the purpose of this project, our own map of the Adriatic Sea was created from a set of 20 Landsat 8 satellite images collected from the website: https://earthexplorer.usgs.gov/

The satellite images were saved in .TIFF format and transferred as such to the QGIS program. They are grouped into one raster layer and form a map that can be seen in Figure 7.

In this project is used WGS84 (*World geodetic system*) with identifier EPSG:4326 was used. WGS84 is the standard in GPS and Google Maps service works on this coordinate reference system. It was required because each exact location was obtained and verified from Google Maps service.

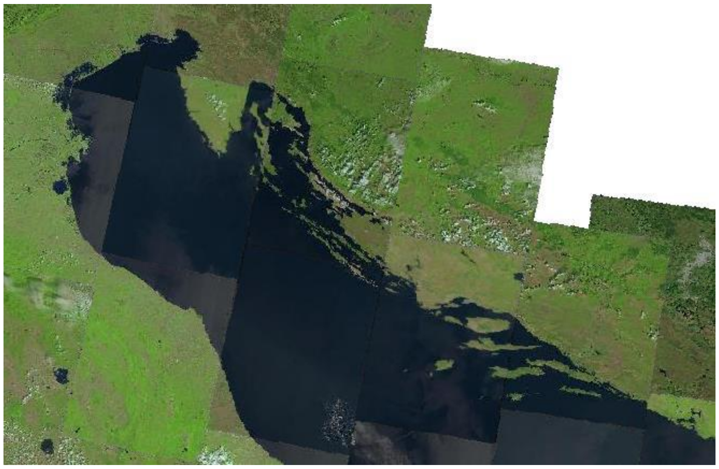

Figure 7 Set of satellite images from the territory of the

Republic of Croatia and Italy

4.3 DATA VISUALIZATION

In order to make the displayed data more understandable to the user, a visible name of the wreck or other feature is added above the symbol, In the project, the table with attributes was additionally modified. A new image attribute was added, which contains the path to the directory where the image is located. After adding a new field to the table, for each feature it was necessary to load an image from the directory in which it is located. The appearance of visualized data can be seen in Figure 8, which shows the southern Adriatic.

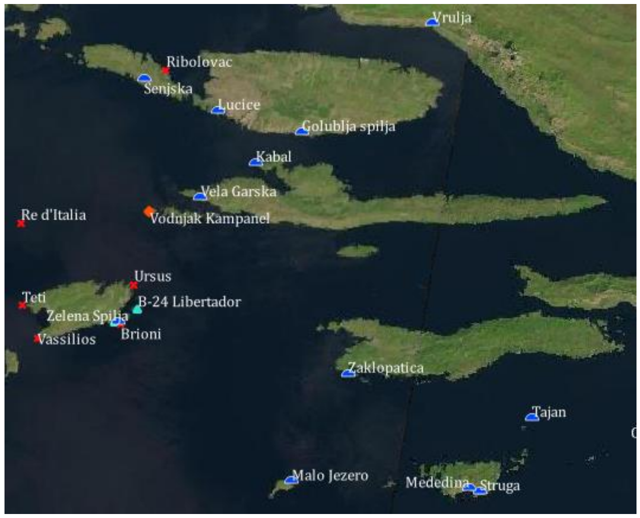

Figure 8 Mapped data of the southern Adriatic islands

The map is exported through the qgis2web plugin. Map can be displayed in a web browser so that it is not necessary to have QGIS software installed to view the map (Figure 9).

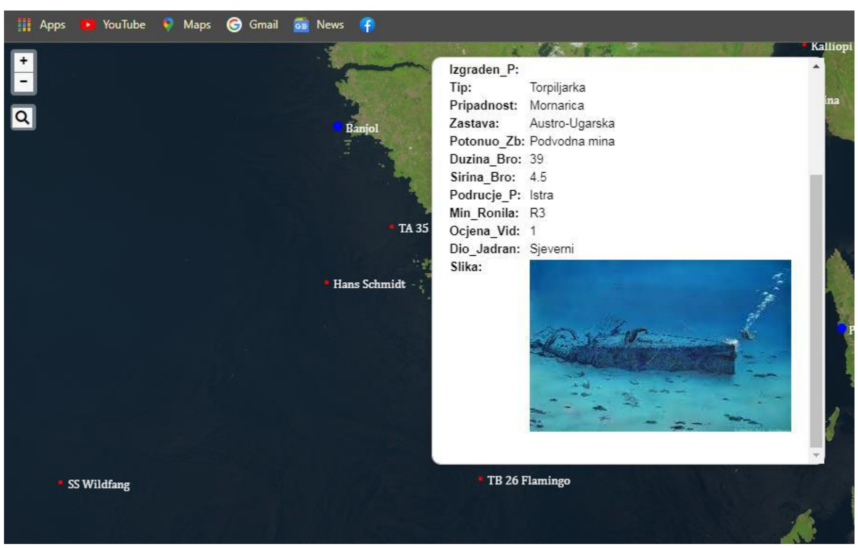

Figure 9 Image display as part of attributes in a Web browser

It is possible to additionally modify the map in such a way as to set the scale, the rotation of the map and the size of the space on which the map is located, as well as the background, frame and grid of the map. By itself, this map doesn't mean much without some context, so it's necessary to add a map legend. The map legend can be further edited by changing the font, spacing and style of the text, and other additional settings. In addition to the legend, a smaller map was added, showing on a larger scale which area it is about. By adding a graphic scale, it is presented the ratio between the distance of the features on the map and in the real world. In the settings, the unit of measurement, segments, width, height and line style can be adjusted if necessary.

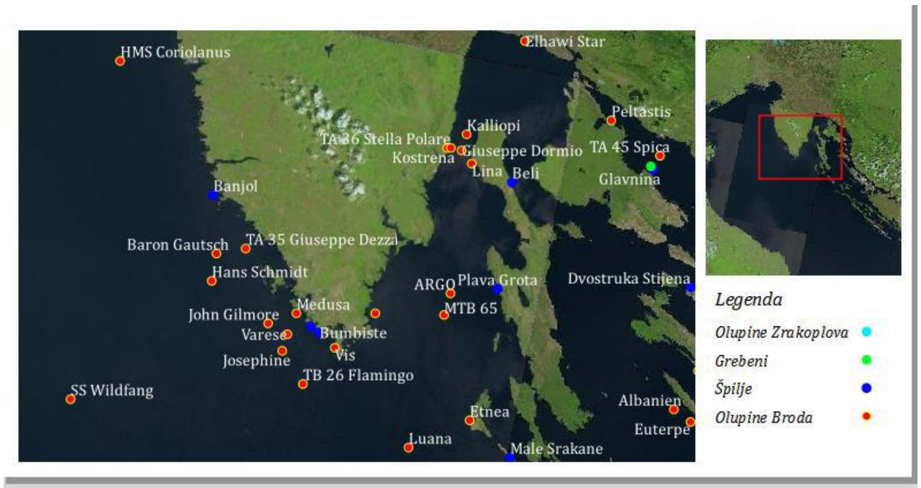

Figure 10 Adding a legend and a smaller map

After completing the creation of the map, it is necessary to export it in the desired format. Some of the formats are JPG, JPEG, TIFF, SVG, PDF. It is also possible to export the data to a table or CSV file in the selected desired resolution, height and width of the page.

5. CONCLUSION

The paper is guided by the idea that such a project can be made as a separate system with the possibility of inclusion in wider and more robust GIS systems. The advantages and benefits of its use are multiple. It can be included in the tourist offer, for example, organized diving activities. Such objects have a significant attraction value. Then, most of these objects have historical significance because they are tied to a particular historical event. And even when the object cannot be tied exactly to a certain date, the possibility of archaeological treatment remains. From the aspect of geodesy as the G part of GIS, such objects are of interest because their location helps to monitor and maintain both objects and locations. It is clear that the sea affects both the location and the integrity of the object. This is intended to emphasize the dynamism of the system in terms of the possibility of intentional or unintentional dislocations of the observed objects. From the aspect of informatics as well as part of GIS, such projects are grateful topics when creating a database, especially in an object-oriented software environment. Vector data is easily arranged as a relational database of Cartesian coordinates and associated attributes, while rasterization can be performed by storing other than primitive data and object-type data such as digitized images. The authors consider the project open for refinement of each targeted and useful type and remains open for possible useful connection or inclusion in wider projects. In this sense, the authors also remain open to all forms of cooperation.

REFERENCES

[1] Pickles, J. (1995.) Representations in an Electronic Age: Geography, GIS, and Democracy, New York: The Guilford Press

[2] Heywood, I., Cornelius, S. and Carver, S. (2006.) An introduction to geographical information systems, 3rd Edition, Harlow: Pearson Education Limited

[3] Bolstad, P. (2016.) GIS fundamentals: A first text on geographic information systems. Eider (PressMinnesota).

[4] Pingel, T. (2018.) The raster data model. *Geographic Information Science & Technology Body of Knowledge*.

[5] Longley, P.A., Goodchild, M.F., Maguire, D.J. and Rhind, D.W. (2005.) *Geographic information systems and science*. John Wiley & Sons.

[6] Frka, D. (2012.) Olupine (nalazi) novovjekih brodova u Jadranskom podmorju, IV. međunarodna konferencija o Industrijskoj baštini, Zbornik radova, Rijeka, Pro Torpedo Rijeka, 2012., http://protorpedo-rijeka.hr/wp/wp-content/uploads/2018/04/62.pdf

[7] Iveša, N., Vojnić, N., Komšo, D. (2015.) Istarska podvodna priča - karta podvodnih arheoloških lokaliteta, (Underwater Story of Istria - map of the underwater archaeological sites), 2015.

[8] Veperdi A., Az Osztrák-Magyar Flotta Tengeralattjárói (Austro-Hungarian Destroyers), https://adoc.pub/az-osztrak-magyar-flotta-tengeralattjaroi-sszeallitotta-vepe.html

[9] Domines Peter, P. (2019.) Pad savezničkog zrakoplova Bristol Beaufightera (nt 997) kod Senja u listopadu 1944. godine, *Senjski zbornik*, 46(1), str. 297-324. https://doi.org/10.31953/sz.46.1.11

Web sources:

H2O Globe [Online] https://h2oglobe.com/ [Accesed: 31.05.2022.]

Ronjenje u Hrvatskoj [Online] http://www.ronjenjehrvatska.com/hr/home [Accesed: 31.05.2022.]

Diving Shark ronilački klub [Online] https://www.diving-shark.hr/en/ [Accesed: 31.05.2022.]

Krnica ronilački klub [Online] https://krnica.com/index.php [Accesed: 31.05.2022.]

Parking system simulation model using CNN

Matej Babič

Faculty of Information Studies, Novo mesto, Slovenia

Abstract

The article shows a possibility of applying graph theory to solving problems in the field of wireless sensor networks. The modernization of the infocommunication infrastructure of the regional data transmission network is presented to increase the maximum transmission speed of existing transport routes, ensure quality of service and reliability. We research one of the fundamental issues in such networks in which we would like to determine whether an area of interest is sufficiently covered by a given set of sensors. The dynamics of car parking is modelled with cellular neural networks that predict the occupancy of a parking lot regards on weather conditional.

1. Introduction

One of the areas of development of the Internet of Things (IoT) is the construction of all-pervasive sensor networks, based on self-organizing wireless networks. WiFi is the industrial name of the technology of wireless data exchange, which belongs to the group of standards for the organization of wireless networks IEEE 802.11. Wireless, all-penetrating sensor networks (BSNs) are self-organizing networks consisting of multiple wireless sensor units distributed in space and designed to monitor and control the characteristics of the environment or objects located in it. The space that is covered by the sensor network is called the sensory field. Wireless sensor nodes are miniaturized devices with limited resources: battery charge, memory capacity, computational capabilities, etc. In wireless communication we have inexpensive wireless nodes capable of sensing, storing, processing, and communicating data. So they are becoming increasingly common and readily available. However, combining a large number of these elements into the network due to the effect of the roving intelligence provides an opportunity to get a real picture of the events and processes occurring within the framework of a sensory field.

The graph theory finds applications, for example, in geoinformation systems. Existing or newly designed houses, structures, quarters, etc. are considered as peaks, and the connecting roads, engineering networks, transmission lines, etc., are like ribs. The application of various calculations made on such a graph allows, for example, to find the shortest bypass or the nearest grocery store, to plan the optimal route. The theory of graphs contains a large number of unresolved problems and not yet proven hypotheses. Know the content of the discipline "Graph Theory" and have a fairly complete idea of its possibilities in other sections of mathematics and in applications; have an idea of the structures of graph theory and the basic combinatorial methods of proof and be able to apply these methods, including in wireless networks. When graphs are depicted in the drawings, the following notation is most often used: the vertices of the graph are represented by dots or, when the vertex's meaning is specified, rectangles, ovals, etc., where the meaning of the vertex (graphs of flowcharts of algorithms) is revealed inside the figure. Cellular automata provide useful models for many studies in natural and computational sciences and combinatorial mathematics; in particular, they represent a natural way of studying the evolution of large physical systems. Cellular automata also form a common parallel computing paradigm, just as Turing machines do for sequential computing . The popularity of cellular automata is based on their comparative simplicity combined with great potential for modeling a set of interconnected homogeneous objects. Each cell represent a finite state machine, whose state is determined by the states of neighboring cells and, possibly, by its own. Changes in the values of all cells occur simultaneously after calculating the new state of each lattice cell. When a lattice is homogeneous, all the cells have the same rule. However, many dynamical systems have continuous cell states and simply cannot use binary values of states. In such cases an extension of cellular automata can be used, cellular neural networks (CNN). In this article, we use cellular neural networks to model the dynamics of a parking lot.

2. Data preparation

In the city Novo mesto, Slovenia, it is parking system with 38 park places. One parking place is reserved for the disabled (yellow circle in Fig. 1) and two places for gas auto. Fig. 5 represent geometry of parking system in the city Novo mesto, Slovenia. Each parking place have magnetic sensor. So, we used data from magnetic sensors. We calculating average degree of occupancy of each of 38 park places for 30 days. Then, we transform this data to matrix with different colors Fig. 2. Table 1 represent weather data for 30 days.

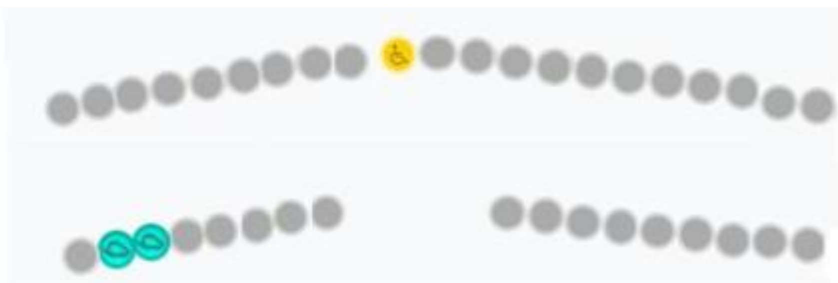

Fig. 1: Geometry of parking

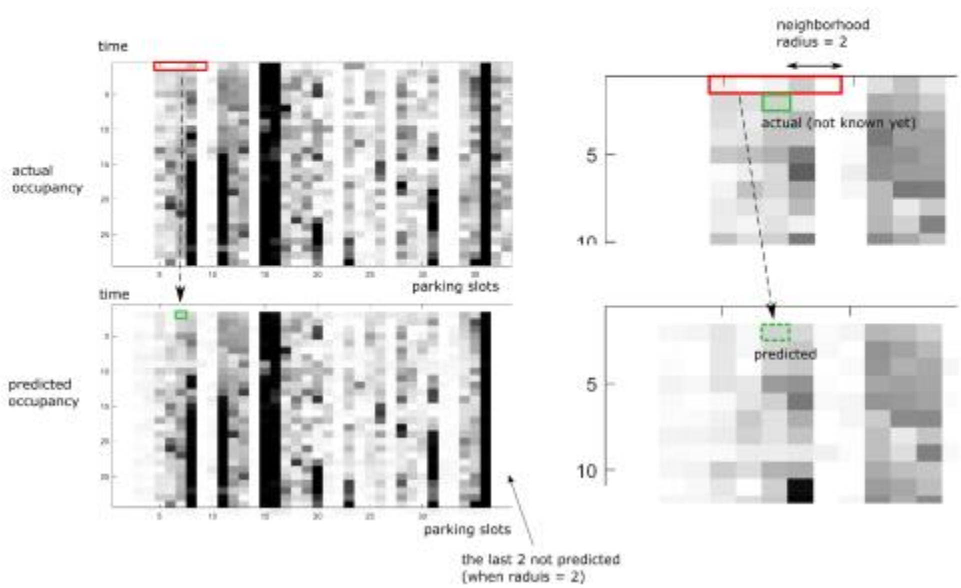

Figure 2: The occupancy of the parking lot and its prediction by CNN, taking also the weather into consideration

	Temperature	Wint	Humidity	Dew point	Pressure	Weather
1	20°C	11 Km/h	69%	14°C	1020,0mb	Clear
2	22°C	13 Km/h	61%	14°C	1016,0mb	Few clouds
3	16°C	0 Km/h	88%	14°C	1016,0mb	Partly cloudy
4	17°C	7 Km/h	77%	13°C	1020,0mb	Few clouds
5	20°C	19 Km/h	64%	13°C	1017,0mb	Few clouds
6	20°C	4 Km/h	60%	12°C	1016,0mb	Few clouds
7	20°C	4 Km/h	69%	14°C	1018,0mb	Few clouds
8	23°C	20 Km/h	65%	16°C	1022,0mb	Few clouds
9	22°C	4 Km/h	65%	15°C	1023,0mb	Clear
10	19°C	6 Km/h	78%	15°C	1021,0mb	Clear
11	19°C	4 Km/h	73%	14°C	1017,0mb	Clear
12	18°C	2 Km/h	68%	12°C	1021,0mb	Clear
13	16°C	7 Km/h	77%	12°C	1024,0mb	Clear
14	19°C	2 Km/h	60%	11°C	1020,0mb	Clear
15	18°C	4 Km/h	64%	11°C	1018,0mb	Clear
16	9°C	9 Km/h	94%	8°C	1019,0mb	Rain
17	8°C	7 Km/h	93%	7°C	1025,0mb	Cloudy
18	8°C	7 Km/h	62%	1°C	1022,0mb	Partly cloudy
19	11°C	6 Km/h	88%	9°C	1007,0mb	Rain
20	21°C	2 Km/h	60%	13°C	996,0mb	Partly cloudy
21	12°C	2 Km/h	100%	12°C	999,0mb	Cloudy
22	19°C	17 Km/h	64%	12°C	998,0mb	Partly cloudy
23	12°C	11 Km/h	88%	10°C	1005,0mb	Partly cloudy
24	11°C	4 Km/h	82%	8°C	1008,0mb	Partly cloudy
25	7°C	4 Km/h	100%	7°C	1007,0mb	Cloudy
26	15°C	7 Km/h	63%	8°C	1008,0mb	Few clouds
27	8°C	6 Km/h	82%	5°C	1011,0mb	Cloudy
28	7°C	2 Km/h	93%	6°C	1017,0mb	Cloudy
29	9°C	6 Km/h	94%	8°C	1006,0mb	Rain
30	9°C	2 Km/h	94%	8°C	998,0mb	Rain

Table 1: Weather data

3. Results and discussion

There are P = 38 parking spaces in the parking lot. The data is available for D = 30 days. For each day, only data of the average occupancy (in percent) for each parking space is given. Therefore, a proper cellular automaton (CA) cannot be used, as it operates above a finite number of states; typically binary states (0 and 1, i.e. unoccupied and occupied). Therefore, s cellular neural network (CNN) is applied here, which, based on the average occupancy of the parking space or cell and the average occupancy of adjacent cells, attempts to predict the average occupancy of the parking space for the next day, as shown in Figure 3. When the rule is the same for all cells, we speak of a homogeneous cellular automaton or homogeneous cellular neural network.

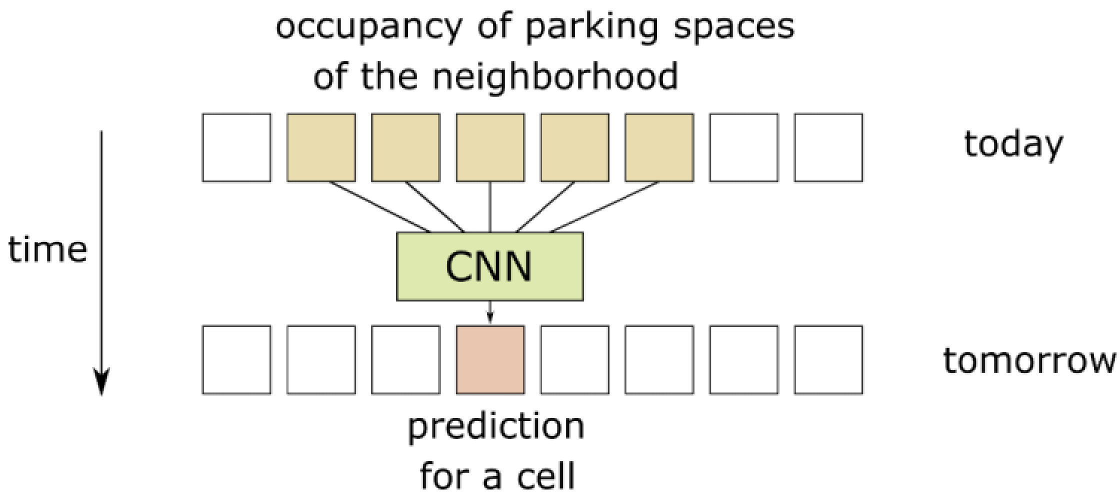

Fig. 3: The occupancy of a parking space is predicted on the basis of the occupancy of the neighborhood a day before. In this case, the radius of the neighborhood or adjacency is 2, giving 1+2*2 = 5 cells.

The error of the CNN prediction is calculated as

$$E_{CNN} = \frac{1}{(D-1)\cdot P}\sum_{i=2}^{D}\sum_{j=1}^{P}\left(x_{ij} - f\left(x_{i-1,j-n}, \dots, x_{i-1,j}, \dots, x_{i-1,j}\right)\right)^2$$

The basic measure of error that every successful model must beat is the error of predicting that the state the next day will be the same as today (in this case % occupancy). Such prediction is called *naive predictor*.

$$E_{naive} = \frac{1}{(D-1)\cdot P}\sum_{i=2}^{D}\sum_{j=1}^{P}\left(x_{ij} - x_{i-1,j}\right)^2$$

In our case, the mean squared error (MSE) is 0.02625. The RMSE (root MSE) is 0.16, i.e. a 16% error in the occupancy prediction.

In CNN training and prediction testing, 10-fold cross-validation was used, meaning that the data set was divided into 10 parts; each time, 90% of the data was used to train the CNN model and 10% (one of 10 subsets) was used for testing. In addition, 10 different experiments with 10-fold cross-validation were done for each model, in order to reduce the effects of random initial weights and of the training procedure. All the models had one output neuron, but differed in the number of hidden layers and hidden neurons. For example, 10-5-1 means 10 neurons in the first hidden layer, 5 in the second, and one in the output layer.

Three different adjacencies are taken: 0, 1 and 2. Adjacency (radius) 2 means that in addition to a cell, we also consider two neighbors on each side. In such a case, two edge cells are not predicted. The spaces in the parking lot were divided into two groups: those that are closer to the entrance / exit of the parking lot, and the others. The two groups are differentiated using an additional input (0 or 1) that can influence the network to implicitly build at least a partially different model. It was found that this helps a little. Another factor that helped in the prediction was the weather data: average dayly values of temperature, wind speed, relative humidity, dew point, air pressure, and weather (qualitatively). Therefore, the actual CNN model included also these additional data, so the CNN function was extended as

$$f\left(x_{i-1,j-n}, \dots, x_{i-1,j}, \dots, x_{i-1,j}, entrance/exit, weather\ data\right)$$

Figure 4. The parking lot. The area closer to the entrance / exit of the parking lot is marked by a white rectangle.

It was found that the appropriate number of training epochs was 100. Namely, with smaller numbers of epochs the CNN was not trained enough, while with larger numbers the CNN began to overfit to the training data, thus deteriorating the test results.

E_{CNN}	neighborhood radius (adjacency)		
	0	**1**	**2**
1	0.0270 ± 0.0001	0.0263 ± 0.0002	0.0262 ± 0.0001
3-1	0.0252 ± 0.0002	0.0299 ± 0.0003	0.0246 ± 0.0005
5-1	0.0233 ± 0.0001	0.0214 ± 0.0003	0.0214 ± 0.0003
10-1	0.0223 ± 0.0004	0.0204 ± 0.0005	0.0177 ± 0.0005
10-5-1	0.0208 ± 0.0006	0.0223 ± 0.0007	0.0179 ± 0.0005
20-10-1	0.0150 ± 0.0012	0.0089 ± 0.0010	0.0141 ± 0.0004
40-20-1	0.0133 ± 0.0012	0.0035 ± 0.0012	**0.0019** ± 0.0008
80-40-1	0.0145 ± 0.0007	0.0067 ± 0.0007	0.0069 ± 0.0010
120-60-1	0.0146 ± 0.0007	0.0081 ± 0.0007	0.0032 ± 0.0006

Table 2. Simulation results of the CNN (MSE and standard error)

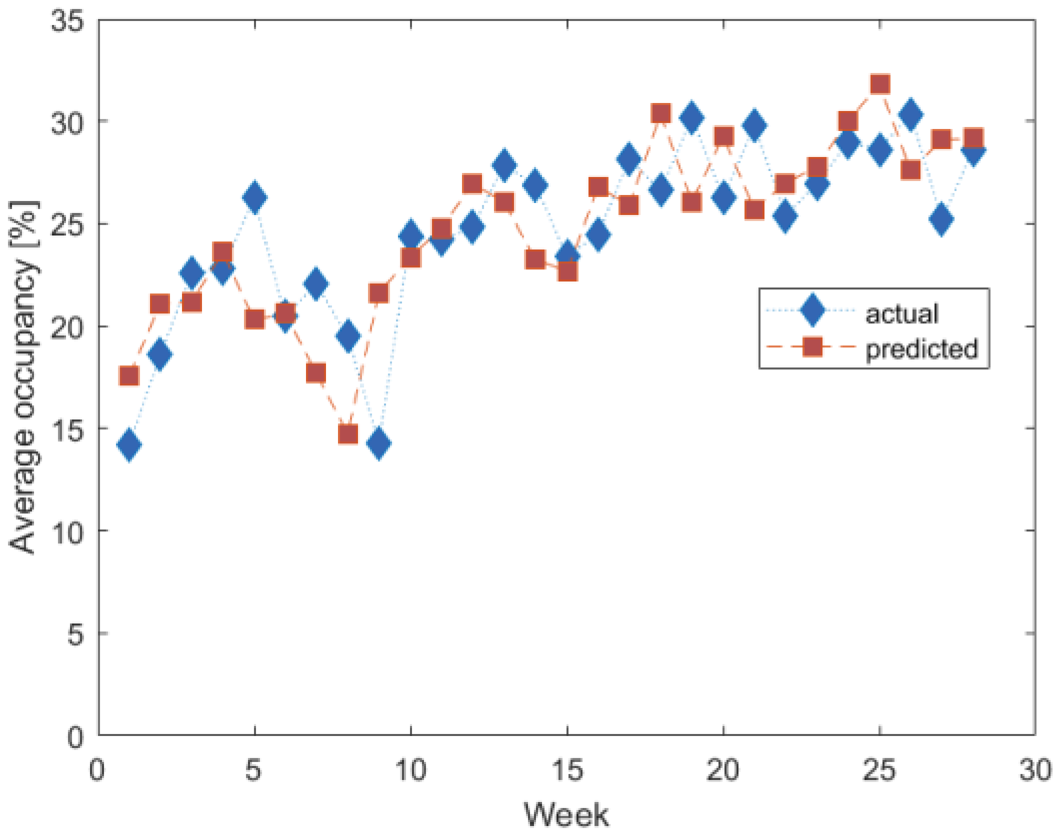

Graph 1: Simulation graph of average occupancy

The results show that it is possible to get much better prediction than the naive one (16%): the best MSE was 0.0019, which yields RMSE of 0.0436, that is below 5%.

Acknowledgement

The investment is co-financed by the Republic of Slovenia and the European Union from the European Regional Development Fund and supported by the Slovenian Research Agency (ARRS).

References

[1] Zhou, Honbo. The Internet of Things in the Cloud: A Middleware Perspective. Boca Raton: CRC Press, Taylor & Francis Group, 2013.
[2] Golbon-Haghighi, M.H. (2016). Beamforming in Wireless Networks (PDF). InTech Open. pp. 163–199. doi:10.5772/66.399. ISBN 9781466557529.

PPT bicycle rental in the GoNM system using Descriptive statistics

Matej Babič

Faculty of Information Studies, Novo mesto, Slovenia

Abstract

This study proposes a descriptive statistics for PPT bicycle rental in the GoNM system in the town of Novo mesto, Slovenia. Public passenger transport (PPT) is important for every municipality, as the current transport system faces well-known problems such as congestion, environmental impact, lack of parking areas, increased safety risks and high energy consumption. Urban transport is crucial for the functionality of any city. High-quality and usable urban transport not only affects the functionality of the city as an economic and social center, but also reduces the number of passenger cars on the streets. The wider Novo mesto region, with about 30,000 inhabitants, is an important industrial center and is heavily dependent on urban traffic. Unfortunately, the urban traffic of Novo mesto still has a relatively weak influence on the transport connectivity of the wider area. The aim of the research is to analyze and model bicycle rentals. Descriptive statistics for PPT bicycle rental in the GoNM system in the town of Novo mesto, Slovenia are used to predict bicycle traffic over 30 weeks. Our approach will also be useful for other Slovenian and foreign cities with similar needs.

Data preparation
Bicycle data

The bicycle rental data was obtained for 14 stations for 35 weeks between 25.3.2019 and 25.11.2019 from the municipality of Novo mesto, Slovenia. The Microsoft Excel software is used to analyze the data, by using the pivot tables. Table 1 presents the numbers of bike rentals for 14 stations for the 13th week. Table 2 presents number of bike rentals for all 35 weeks. In Table 2 the first column present number of week. Second column present number of rent a bike.

S	**1**	**2**	**3**	**4**	**5**	**6**	**7**	**8**	**9**	**10**	**11**	**12**	**13**	**14**
1	3	4	3	0	3	2	0	1	2	1	2	5	0	3
2	3	1	2	8	2	2	0	5	4	0	0	1	1	1
3	4	1	4	0	3	1	7	2	0	0	1	3	0	0
4	3	6	1	5	3	0	2	1	3	1	0	2	2	4
5	1	3	7	1	13	13	0	3	1	1	1	11	0	1
6	1	2	2	0	14	7	3	2	3	0	1	5	1	2
7	0	0	6	3	1	3	4	0	0	0	1	0	0	0
8	5	2	1	4	2	0	0	8	3	1	0	3	5	3
9	1	1	0	5	0	1	1	3	7	1	0	2	0	3
10	1	1	0	1	2	1	0	0	1	2	0	0	0	0
11	2	0	1	0	0	2	0	0	1	0	26	0	1	0
12	10	2	4	1	10	2	0	1	3	1	0	11	0	0
13	0	1	1	1	0	2	0	6	0	0	0	0	5	4
14	6	0	0	0	2	3	3	1	3	0	0	1	5	4

Table 2: Numbers of bike rentals for 14 stations for the 13th week

# week	1	2	3	4	5	6	7	8	9	10	11	12	13	14	15	16	17	18
# rent a bike	18	13	88	142	193	27	106	78	252	190	353	413	432	367	361	291	301	241
# week	19	20	21	22	23	24	25	26	27	28	29	30	31	32	33	34	35	
# rent a bike	204	238	189	267	249	256	256	226	221	293	280	184	275	86	58	63	31	

Table 2: Number of rent a bike for 35 weeks

Weather data

The weather data were obtained, such as temperature (T), rainfall (R), wind speed (W), and relative humidity (H), from Weather Society Zeus, Slovenia, for each day. The averages of all data were calculated for 35 weeks. Table 3 shows the weather data. The first column (n) contains the number of the week, the second column average temperature [°C], the third column average rainfall [mm], the fourth column average wind speed [m/s] and the fifth column average relative humidity [%].

n	T	R	W	H
1	11.3	0.0	4.6	55.3
2	10.2	0.1	8.3	63.3
3	12.3	1.1	5.5	72.8
4	9.3	3.7	4.7	86.2
5	14.0	0.0	6.1	55.9
6	15.9	2.1	6.3	69.6
7	13.1	1.6	4.7	73.7
8	13.2	0.6	4.1	71.9
9	10.8	6.7	4.7	83.8
10	18.4	0.0	3.9	67.9
11	16.9	8.3	1.9	82.3
12	24.4	0.0	3.9	60.5
13	26.8	0.0	3.7	61.4
14	23.0	3.5	3.2	76.9
15	26.6	0.1	4.3	60.7
16	25.7	2.1	4.4	65.8
17	20.1	0.7	3.9	73.5
18	24.1	0.1	2.5	61.0
19	26.5	3.6	2.6	68.2
20	23.6	2.0	2.0	75.7
21	26.1	0.1	3.9	67.1
22	22.4	3.2	3.0	71.5
23	23.1	0.8	4.1	75.7
24	24.9	0.1	2.0	78.1
25	18.1	1.7	4.5	80.7
26	18.3	1.3	2.4	77.4

27	15.3	1.9	4.1	75.3
28	16.5	1.7	2.1	84.7
29	15.4	1.7	3.0	77.3
30	13.7	3.0	4.9	80.3
31	16.6	0.4	3.0	79.9
32	16.6	0.2	1.6	79.4
33	9.7	1.3	4.6	89.0
34	9.3	4.0	2.3	92.8
35	9.0	3.3	3.1	91.5

Table 3: Weather conditions parameters

Results

Descriptive Statistics Report

Dataset Untitled

Summary Section of T

Count	Mean	Standard Deviation	Standard Error	Minimum	Maximum	Range
35	177,4857	58,84245	9,946189	90	268	178

Counts Section of T

Rows	Sum of Frequencies	Missing Values	Distinct Values	Sum	Total Sum Squares	Adjusted Sum Squares
35	35	0	33	6212	1220264	117722,7

Means Section of T

Parameter	Mean	Median	Geometric Mean	Harmonic Mean	Sum	Mode
Value	177,4857	166	167,5821	157,6626	6212	
Std Error	9,946189				348,1166	
95% LCL	157,2726	140	148,5405	140,1752	5504,542	
95% UCL	197,6988	224	189,0646	180,1351	6919,458	
T-Value	17,84459					
Prob Level	0					
Count	35		35	35		0

Variation Section of T

Parameter	Variance	Standard Deviation	Unbiased Std Dev	Std Error of Mean	Interquartile Range	Range
Value	3462,434	58,84245	59,27665	9,946189	105	178
Std Error	486,0747	5,841136		0,9873322		
95% LCL	2265,38	47,59601		8,045195		
95% UCL	5943,716	77,0955		13,03152		

Skewness and Kurtosis Section of T

Parameter	Skewness	Kurtosis	Skewness (Fisher's g1)	Kurtosis (Fisher's g2)	Coefficient of Variation	Coefficient of Dispersion
Value	0,1133043	1,689781	0,1184421	-1,325481	0,3315334	0,2984509
Std Error	0,249156	0,202497			0,02757887	

Trimmed Section of T

Parameter	5% Trimmed	10% Trimmed	15% Trimmed	25% Trimmed	35% Trimmed	45% Trimmed
Trim-Mean	177,2937	177,0714	176,7653	175,2429	170,7143	167,8571
Trim-Std Dev	54,51591	49,20699	43,33707	31,9367	13,96666	4,622924
Count	32	28	25	18	11	4

Trimmed Section of T

Parameter	5% Trimmed	10% Trimmed	15% Trimmed	25% Trimmed	35% Trimmed	45% Trimmed
Trim-Mean	177,2937	177,0714	176,7653	175,2429	170,7143	167,8571
Trim-Std Dev	54,51591	49,20699	43,33707	31,9367	13,96666	4,622924
Count	32	28	25	18	11	4

Mean-Deviation Section of T

Parameter	|X-Mean|	|X-Median|	(X-Mean)^2	(X-Mean)^3	(X-Mean)^4
Average	50,35592	49,54286	3363,507	22102,18	1,911679E+07
Std Error	5,985037		472,1869	47716,13	3691590

Quartile Section of T

Parameter	10th Percentile	25th Percentile	50th Percentile	75th Percentile	90th Percentile
Value	95,4	131	166	236	262,6
95% LCL	90	97	140	184	241
95% UCL	123	154	224	261	268

Normality Test Section of T

Test Name	Test Value	Prob Level	10% Critical Value	5% Critical Value	Decision (5%)
Shapiro-Wilk W	0,9260323	0,02135616			Reject normality
Anderson-Darling	0,7675943	0,04607262			Reject normality
Martinez-Iglewicz	0,9689438		1,129221	1,196894	Can't reject normality
Kolmogorov-Smirnov	0,1001901		0,136	0,148	Can't reject normality
D'Agostino Skewness	0,3147062	0,7529847	1,645	1,96	Can't reject normality
D'Agostino Kurtosis	-3,2064	0,001344	1,645	1,96	Reject normality
D'Agostino Omnibus	10,3803	0,005571	4,605	5,991	Reject normality

Plots Section of T

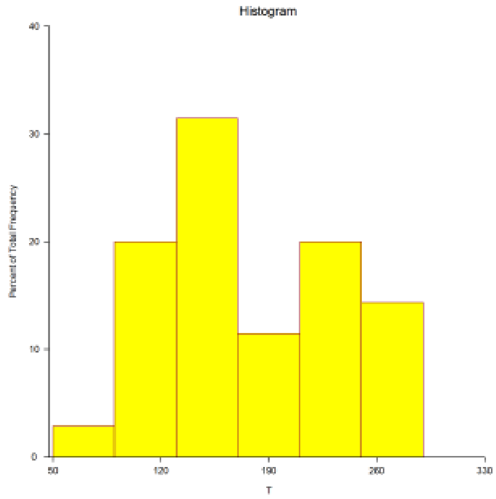

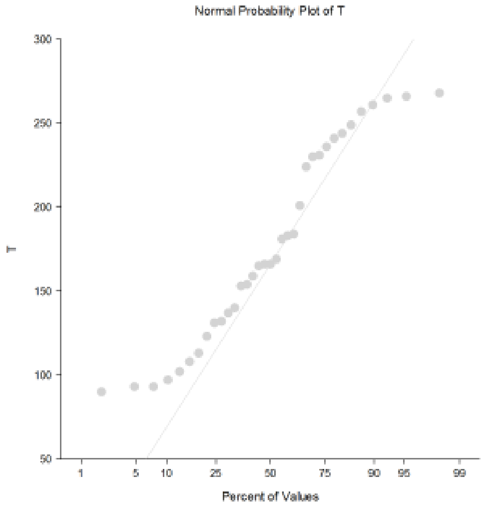

Percentile Section of T

Percentile	Value	95% LCL	95% UCL	Exact Conf. Level
99	268			
95	266,4			
90	262,6	241	268	95,49782
85	253,8	230	266	96,4725
80	243,4	201	265	96,67783
75	236	184	261	95,00591
70	230,2	169	249	95,71412
65	210,2	166	244	96,80229
60	183,6	159	236	96,0789
55	178,6	154	231	95,92338
50	166	140	224	95,90404
45	165,2	132	184	95,92338
40	156	123	181	95,97847
35	147,8	113	169	96,80229
30	136	102	165	95,5
25	131	97	154	95,00591
20	115	93	140	96,16875
15	104,4	90	132	96,74316
10	95,4	90	123	95,49782
5	92,4			
1	90			

Percentile Formula: Ave X(p[n+1])

Stem-Leaf Plot Section of T

Depth	Stem	Leaf
4	.	9999
7	1*	001
11	T	2333
15	F	4555
(4)	S	6666
16	.	888
13	2*	0
12	T	2333
8	F	4445
4	S	6666

Unit = 10 Example: 1| 2 Represents 120

Dataset Untitled

Summary Section of R

Count	Mean	Standard Deviation	Standard Error	Minimum	Maximum	Range
35	17,42857	19,28774	3,260223	0	83	83

Counts Section of R

Rows	Sum of Frequencies	Missing Values	Distinct Values	Sum	Total Sum Squares	Adjusted Sum Squares
35	35	0	23	610	23280	12648,57

Means Section of R

Parameter	Mean	Median	Geometric Mean	Harmonic Mean	Sum	Mode
Value	17,42857	13	11,07896	4,227522	610	
Std Error	3,260223				114,1078	
95% LCL	10,803	4	6,713369	2,696951	378,1051	
95% UCL	24,05414	20	18,28342	9,775044	841,895	
T-Value	5,345822					
Prob Level	6,106905E-06					
Count	35		30	30		0

Variation Section of R

Parameter	Variance	Standard Deviation	Unbiased Std Dev	Std Error of Mean	Interquartile Range	Range
Value	372,0168	19,28774	19,43006	3,260223	29	83
Std Error	136,8766	5,018025		0,848201		
95% LCL	243,4009	15,60131		2,637103		
95% UCL	638,6151	25,27083		4,271551		

Skewness and Kurtosis Section of R

Parameter	Skewness	Kurtosis	Skewness (Fisher's g1)	Kurtosis (Fisher's g2)	Coefficient of Variation	Coefficient of Dispersion
Value	1,600727	5,738066	1,673311	3,366849	1,106673	1,065934
Std Error	0,3398075	1,622535			0,1482705	

Trimmed Section of R

Parameter	5% Trimmed	10% Trimmed	15% Trimmed	25% Trimmed	35% Trimmed	45% Trimmed
Trim-Mean	15,13492	14,33929	13,79592	12,61429	13,11905	14
Trim-Std Dev	13,8003	11,95714	10,6541	7,116547	4,420064	2,04939
Count	32	28	25	18	11	4

Mean-Deviation Section of R

Parameter	|X-Mean|	|X-Median|	(X-Mean)^2	(X-Mean)^3	(X-Mean)^4
Average	14,13878	13,85714	361,3878	10997,08	749397,8
Std Error	1,961812		132,9658	6300,914	452079,3

Quartile Section of R

Parameter	10th Percentile	25th Percentile	50th Percentile	75th Percentile	90th Percentile
Value	0	1	13	30	38,2
95% LCL	0	0	4	17	32
95% UCL	1	7	20	37	83

Normality Test Section of R

Test Name	Test Value	Prob Level	10% Critical Value	5% Critical Value	Decision (5%)
Shapiro-Wilk W	0,8208777	5,381184E-05			Reject normality
Anderson-Darling	1,715375	0,0002150494			Reject normality
Martinez-Iglewicz	1,528559		1,129221	1,196894	Reject normality
Kolmogorov-Smirnov	0,1694067		0,136	0,148	Reject normality
D'Agostino Skewness	3,555084	0,0003778588	1,645	1,96	Reject normality
D'Agostino Kurtosis	2,6399	0,008294	1,645	1,96	Reject normality
D'Agostino Omnibus	19,6075	0,000055	4,605	5,991	Reject normality

Plots Section of R

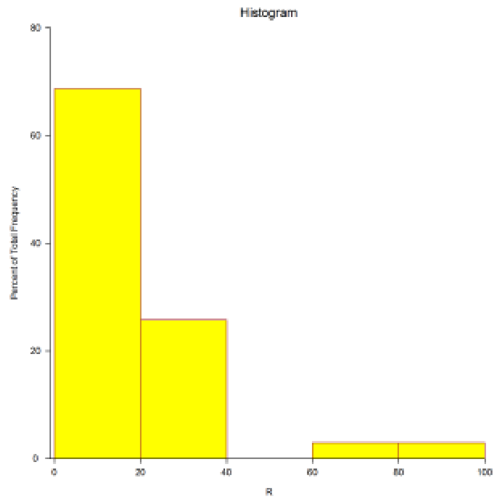

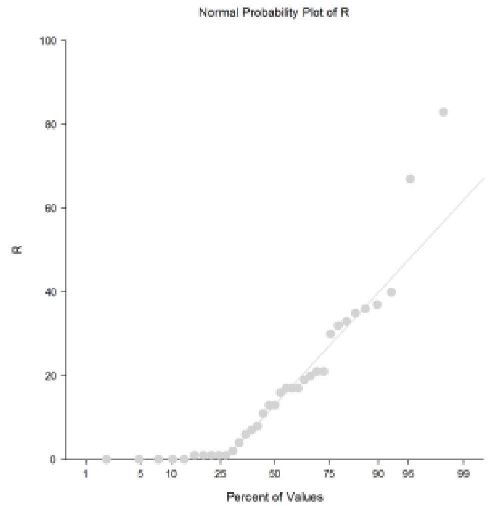

Percentile Section of R

Percentile	Value	95% LCL	95% UCL	Exact Conf. Level
99	83			
95	70,2			
90	38,2	32	83	95,49782
85	35,6	21	67	96,4725
80	32,8	19	40	96,67783
75	30	17	37	95,00591
70	21	16	35	95,71412
65	19,4	13	33	96,80229
60	17	8	30	96,0789
55	16,8	7	21	95,92338
50	13	4	20	95,90404
45	11,4	1	17	95,92338
40	7,4	1	17	95,97847
35	5,2	1	16	96,80229
30	1,8	0	11	95,5
25	1	0	7	95,00591
20	1	0	4	96,16875
15	0,4	0	1	96,74316
10	0	0	1	95,49782
5	0			
1	0			

Percentile Formula: Ave X(p[n+1])

Stem-Leaf Plot Section of R

Depth	Stem	Leaf
12	0*	000001111124
15	.	678
(3)	1*	133
17	.	67779
12	2*	011
9	.	
9	3*	023
6	.	567
3	4*	0
High		67, 83

Unit = 1 Example: 1| 2 Represents 12

Summary Section of Y

Count	Mean	Standard Deviation	Standard Error	Minimum	Maximum	Range
35	206,9143	115,3874	19,50403	13	432	419

Counts Section of Y

Rows	Sum of Frequencies	Missing Values	Distinct Values	Sum	Total Sum Squares	Adjusted Sum Squares
35	35	0	34	7242	1951158	452684,8

Means Section of Y

Parameter	Mean	Median	Geometric Mean	Harmonic Mean	Sum	Mode
Value	206,9143	226	157,7973	91,97581	7242	256
Std Error	19,50403				682,6412	
95% LCL	167,2773	184	115,7374	61,00638	5854,706	
95% UCL	246,5513	256	215,1422	186,807	8629,294	
T-Value	10,60879					
Prob Level	2,513545E-12					
Count	35		35	35		2

Variation Section of Y

Parameter	Variance	Standard Deviation	Unbiased Std Dev	Std Error of Mean	Interquartile Range	Range
Value	13314,26	115,3874	116,2389	19,50403	192	419
Std Error	2440,44	14,95528		2,527904		
95% LCL	8711,173	93,33366		15,77627		
95% UCL	22855,65	151,1808		25,55423		

Skewness and Kurtosis Section of Y

Parameter	Skewness	Kurtosis	Skewness (Fisher's g1)	Kurtosis (Fisher's g2)	Coefficient of Variation	Coefficient of Dispersion
Value	-0,07764058	2,1759	-0,08116117	-0,7620253	0,5576581	0,4088496
Std Error	0,2334829	0,3161589			0,07533523	

Trimmed Section of Y

Parameter	5% Trimmed	10% Trimmed	15% Trimmed	25% Trimmed	35% Trimmed	45% Trimmed
Trim-Mean	205,5159	206,2857	207,2653	216,0571	223,5952	227,5
Trim-Std Dev	100,1207	86,26117	72,24759	48,42923	25,35854	11,634
Count	32	28	25	18	11	4

Mean-Deviation Section of Y

Parameter	|X-Mean|	|X-Median|	(X-Mean)^2	(X-Mean)^3	(X-Mean)^4
Average	93,75021	92,4	12933,85	-114203,8	3,639942E+08
Std Error	11,73639		2370,713	331309,4	1,014974E+08

Quartile Section of Y

Parameter	10th Percentile	25th Percentile	50th Percentile	75th Percentile	90th Percentile
Value	29,4	88	226	280	363,4
95% LCL	13	31	184	252	291
95% UCL	86	190	256	361	432

Normality Test Section of Y

Test Name	Test Value	Prob Level	10% Critical Value	5% Critical Value	Decision (5%)
Shapiro-Wilk W	0,958122	0,2007245			Can't reject normality
Anderson-Darling	0,5202922	0,1859641			Can't reject normality
Martinez-Iglewicz	0,9135617		1,129221	1,196894	Can't reject normality
Kolmogorov-Smirnov	0,1057705		0,136	0,148	Can't reject normality
D'Agostino Skewness	-0,2158599	0,8290969	1,645	1,96	Can't reject normality
D'Agostino Kurtosis	-1,1913	0,233544	1,645	1,96	Can't reject normality
D'Agostino Omnibus	1,4657	0,480527	4,605	5,991	Can't reject normality

Plots Section of Y

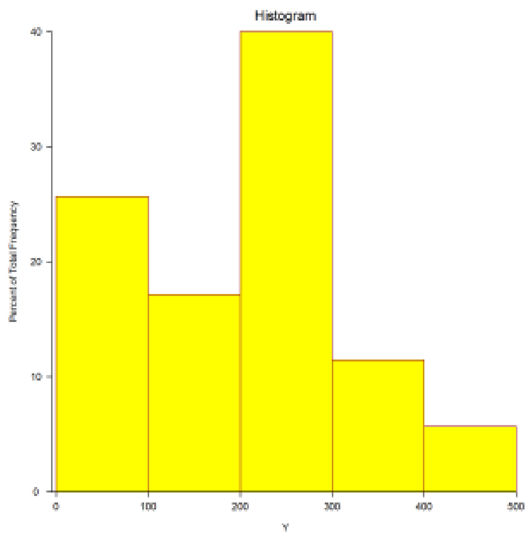

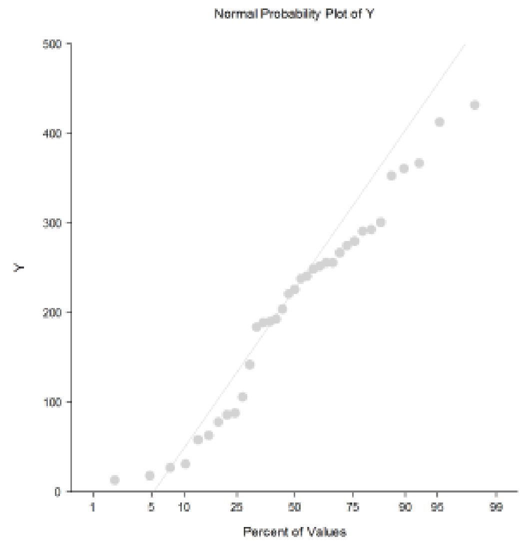

Percentile Section of Y

Percentile	Value	95% LCL	95% UCL	Exact Conf. Level
99	432			
95	416,8			
90	363,4	291	432	95,49782
85	332,2	267	413	96,4725
80	292,6	256	367	96,67783
75	280	252	361	95,00591
70	268,6	238	301	95,71412
65	256	221	293	96,80229
60	250,8	193	280	96,0789
55	240,4	190	275	95,92338
50	226	184	256	95,90404
45	207,4	106	252	95,92338
40	191,2	86	241	95,97847
35	187	78	238	96,80229
30	134,8	58	204	95,5
25	88	31	190	95,00591
20	79,6	18	184	96,16875
15	60	13	106	96,74316
10	29,4	13	86	95,49782
5	17			
1	13			

Percentile Formula: Ave X(p[n+1])

Stem-Leaf Plot Section of Y

Depth	Stem	Leaf
4	0*	1123
9	.	56788
11	1*	04
15	.	8899
(6)	2*	022344
14	.	55567899
6	3*	0
5	.	566
2	4*	13

Unit = 10   Example: 1| 2 Represents 120

Summary Section of W

Count	Mean	Standard Deviation	Standard Error	Minimum	Maximum	Range
35	38,25714	14,23819	2,406693	16	83	67

Counts Section of W

Rows	Sum of Frequencies	Missing Values	Distinct Values	Sum	Total Sum Squares	Adjusted Sum Squares
35	35	0	24	1339	58119	6892,686

Means Section of W

Parameter	Mean	Median	Geometric Mean	Harmonic Mean	Sum	Mode
Value	38,25714	39	35,75536	33,30019	1339	39
Std Error	2,406693				84,23427	
95% LCL	33,36615	30	31,39148	29,2976	1167,815	
95% UCL	43,14813	44	40,7259	38,56949	1510,185	
T-Value	15,89614					
Prob Level	0					
Count	35		35	35		4

Variation Section of W

Parameter	Variance	Standard Deviation	Unbiased Std Dev	Std Error of Mean	Interquartile Range	Range
Value	202,726	14,23819	14,34325	2,406693	20	67
Std Error	60,8057	3,019774		0,510435		
95% LCL	132,6384	11,51687		1,946707		
95% UCL	348,0055	18,65491		3,153255		

Skewness and Kurtosis Section of W

Parameter	Skewness	Kurtosis	Skewness (Fisher's g1)	Kurtosis (Fisher's g2)	Coefficient of Variation	Coefficient of Dispersion
Value	0,8022477	4,148745	0,8386254	1,524681	0,3721707	0,2754579
Std Error	0,3990506	0,9378234			0,0498313	

Trimmed Section of W

Parameter	5% Trimmed	10% Trimmed	15% Trimmed	25% Trimmed	35% Trimmed	45% Trimmed
Trim-Mean	37,4127	37,125	37,32653	38	38,42857	39,14286
Trim-Std Dev	10,91793	9,065732	7,818112	5,694229	3,577288	0,6094494
Count	32	28	25	18	11	4

Mean-Deviation Section of W

Parameter	|X-Mean|	|X-Median|	(X-Mean)^2	(X-Mean)^3	(X-Mean)^4
Average	10,84898	10,74286	196,9339	2217,12	160900,6
Std Error	1,448208		59,06839	1873,564	102355,6

Quartile Section of W

Parameter	10th Percentile	25th Percentile	50th Percentile	75th Percentile	90th Percentile
Value	20	26	39	46	57,4
95% LCL	16	20	30	41	47
95% UCL	25	32	44	55	83

Normality Test Section of W

Test Name	Test Value	Prob Level	10% Critical Value	5% Critical Value	Decision (5%)
Shapiro-Wilk W	0,9403747	0,05744749			Can't reject normality
Anderson-Darling	0,5268898	0,179072			Can't reject normality
Martinez-Iglewicz	1,103379		1,129221	1,196894	Can't reject normality
Kolmogorov-Smirnov	0,1267364		0,136	0,148	Can't reject normality
D'Agostino Skewness	2,064366	0,03898307	1,645	1,96	Reject normality
D'Agostino Kurtosis	1,6958	0,089930	1,645	1,96	Can't reject normality
D'Agostino Omnibus	7,1372	0,028195	4,605	5,991	Reject normality

Plots Section of W

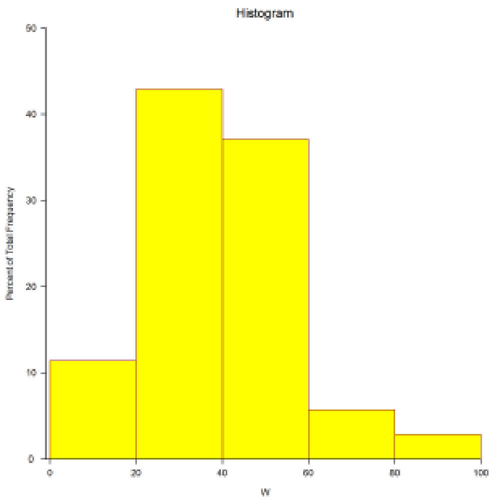

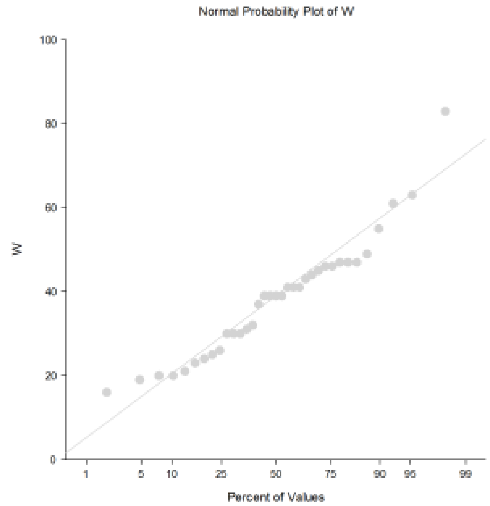

Percentile Section of W

Percentile	Value	95% LCL	95% UCL	Exact Conf. Level
99	83			
95	67			
90	57,4	47	83	95,49782
85	48,2	45	63	96,4725
80	47	43	61	96,67783
75	46	41	55	95,00591
70	45,2	39	47	95,71412
65	43,4	39	47	96,80229
60	41	37	46	96,0789
55	40,6	32	46	95,92338
50	39	30	44	95,90404
45	39	30	41	95,92338
40	34	25	41	95,97847
35	30,6	24	39	96,80229
30	30	21	39	95,5
25	26	20	32	95,00591
20	24,2	19	30	96,16875
15	21,8	16	30	96,74316
10	20	16	25	95,49782
5	18,4			
1	16			

Percentile Formula: Ave X(p[n+1])

Stem-Leaf Plot Section of W

Depth	Stem	Leaf
2	1.	69
7	2*	00134
9	.	56
14	3*	00012
(5)	.	79999
16	4*	11134
11	.	5667779
4	5*	
4	.	5
3	6*	13
High		83

Unit = 1 Example: 1| 2 Represents 12

Summary Section of H

Count	Mean	Standard Deviation	Standard Error	Minimum	Maximum	Range
35	739,1714	97,2049	16,43063	553	928	375

Counts Section of H

Rows	Sum of Frequencies	Missing Values	Distinct Values	Sum	Total Sum Squares	Adjusted Sum Square
35	35	0	34	25871	1,944436E+07	321259

Means Section of H

Parameter	Mean	Median	Geometric Mean	Harmonic Mean	Sum	Mode
Value	739,1714	753	732,8221	726,3392	25871	757
Std Error	16,43063				575,072	
95% LCL	705,7804	696	699,7764	693,5904	24702,31	
95% UCL	772,5625	781	767,4283	762,334	27039,69	
T-Value	44,98741					
Prob Level	0					
Count	35		35	35		2

Variation Section of H

Parameter	Variance	Standard Deviation	Unbiased Std Dev	Std Error of Mean	Interquartile Range	Range
Value	9448,793	97,2049	97,92217	16,43063	132	375
Std Error	1859,703	13,52821		2,286685		
95% LCL	6182,1	78,62633		13,29028		
95% UCL	16220,08	127,3581		21,52744		

Skewness and Kurtosis Section of H

Parameter	Skewness	Kurtosis	Skewness (Fisher's g1)	Kurtosis (Fisher's g2)	Coefficient of Variation	Coefficient of Dispersion
Value	-0,07448594	2,355821	-0,07786348	-0,5534802	0,1315052	0,1030544
Std Error	0,2363352	0,334245			0,01343689	

Trimmed Section of H

Parameter	5% Trimmed	10% Trimmed	15% Trimmed	25% Trimmed	35% Trimmed	45% Trimmed
Trim-Mean	739,1905	738,8036	740,0816	743,8	747,119	748,5714
Trim-Std Dev	81,66502	69,53082	58,18782	38,22247	20,77347	10,73978
Count	32	28	25	18	11	4

Mean-Deviation Section of H

Parameter	|X-Mean|	|X-Median|	(X-Mean)^2	(X-Mean)^3	(X-Mean)^4
Average	77,9951	77,6	9178,828	-65502,09	1,9848E+08
Std Error	9,886995		1806,568	204959,9	6,001398E+07

Quartile Section of H

Parameter	10th Percentile	25th Percentile	50th Percentile	75th Percentile	90th Percentile
Value	606,2	671	753	803	873,2
95% LCL	553	607	696	773	807
95% UCL	658	719	781	862	928

Normality Test Section of H

Test Name	Test Value	Prob Level	10% Critical Value	5% Critical Value	Decision (5%)
Shapiro-Wilk W	0,9811119	0,7947596			Can't reject normality
Anderson-Darling	0,1901875	0,8990407			Can't reject normality
Martinez-Iglewicz	0,9693239		1,129221	1,196894	Can't reject normality
Kolmogorov-Smirnov	0,07250457		0,136	0,148	Can't reject normality
D'Agostino Skewness	-0,2071036	0,835929	1,645	1,96	Can't reject normality
D'Agostino Kurtosis	-0,7124	0,476223	1,645	1,96	Can't reject normality
D'Agostino Omnibus	0,5504	0,759423	4,605	5,991	Can't reject normality

Plots Section of H

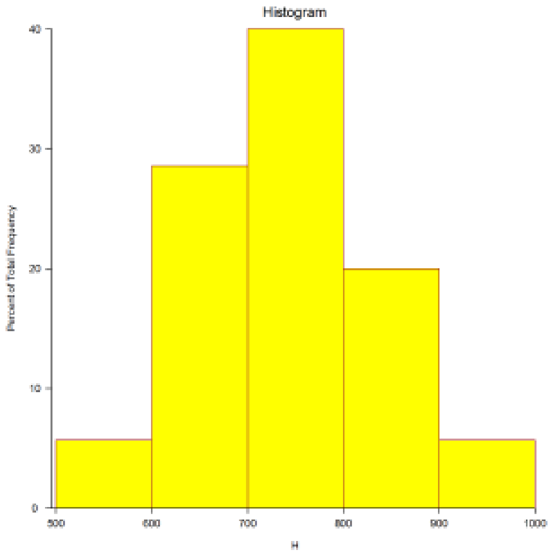

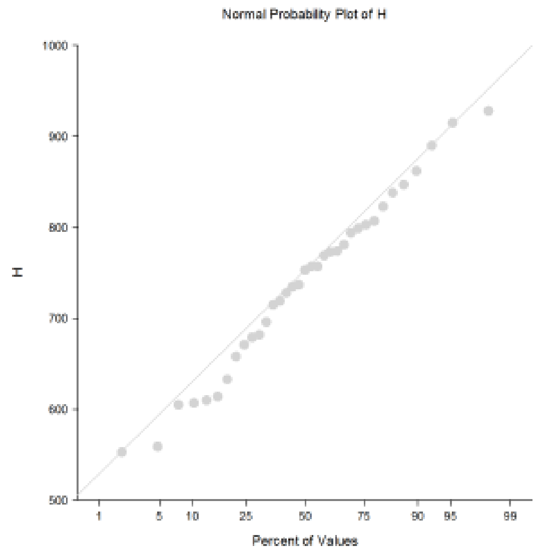

Percentile Section of H

Percentile	Value	95% LCL	95% UCL	Exact Conf. Le
99	928			
95	917,6			
90	873,2	807	928	95,49782
85	843,4	794	915	96,4725
80	819,8	774	890	96,67783
75	803	773	862	95,00591
70	795	757	838	95,71412
65	776,8	737	823	96,80229
60	771,4	728	803	96,0789
55	757	719	799	95,92338
50	753	696	781	95,90404
45	735,4	679	773	95,92338
40	722,6	658	757	95,97847
35	707,4	633	757	96,80229
30	681,4	610	735	95,5
25	671	607	719	95,00591
20	638	559	696	96,16875
15	611,6	553	679	96,74316
10	606,2	553	658	95,49782
5	557,8			
1	553			

Percentile Formula: Ave X(p[n+1])

Stem-Leaf Plot Section of H ————————

Depth	Stem	Leaf
2	5.	55
7	6*	00113
12	.	57789
17	7*	11233
(9)	.	555677899
9	8*	00234
4	.	69
2	9*	12

Unit = 10 Example: 1| 2 Represents 120

Statistics

Variable	Count	Missing	Sum	Mean	SD	SE
T	35	0	6212	177,4857	58,84245	9,946189
R	35	0	610	17,42857	19,28774	3,260223
W	35	0	1339	38,25714	14,23819	2,406693
H	35	0	25871	739,1714	97,2049	16,43063
Y	35	0	7242	206,9143	115,3874	19,50403

Statistics

Variable	95% LCL Mean	95% UCL Mean	Median	Minimum	Maximum	Range
T	157,2726	197,6988	166	90	268	178
R	10,803	24,05414	13	0	83	83
W	33,36615	43,14813	39	16	83	67
H	705,7804	772,5625	753	553	928	375
Y	167,2773	246,5513	226	13	432	419

Statistics

Variable	IQR	10th Pctile	25th Pctile	75th Pctile	90th Pctile	Variance
T	105	95,4	131	236	262,6	3462,434
R	29	0	1	30	38,2	372,0168
W	20	20	26	46	57,4	202,726
H	132	606,2	671	803	873,2	9448,793
Y	192	29,4	88	280	363,4	13314,26

Statistics

Variable	MAD	MADM	COV	COD	Skewness	Kurtosis
T	50,35592	49,54286	0,3315334	0,2984509	0,1133043	1,689781
R	14,13878	13,85714	1,106673	1,065934	1,600727	5,738066
W	10,84898	10,74286	0,3721707	0,2754579	0,8022477	4,148745
H	77,9951	77,6	0,1315052	0,1030544	-0,07448594	2,355821
Y	93,75021	92,4	0,5576581	0,4088496	-0,07764058	2,1759

Plots of each Statistic

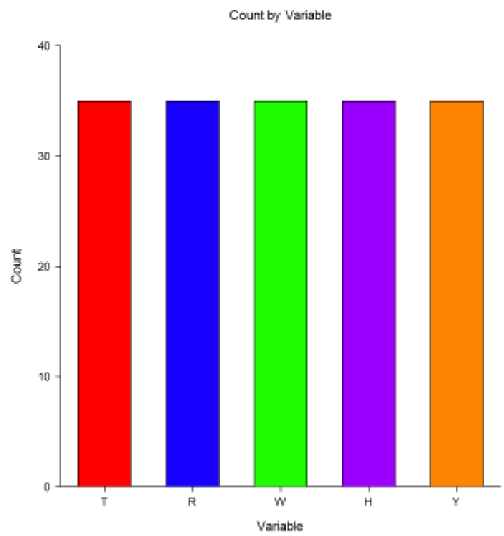

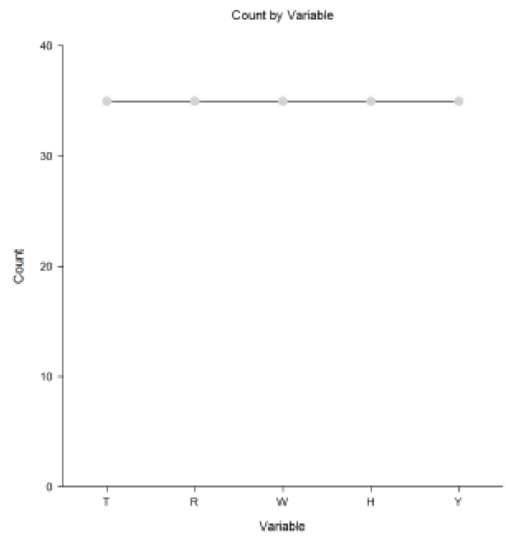

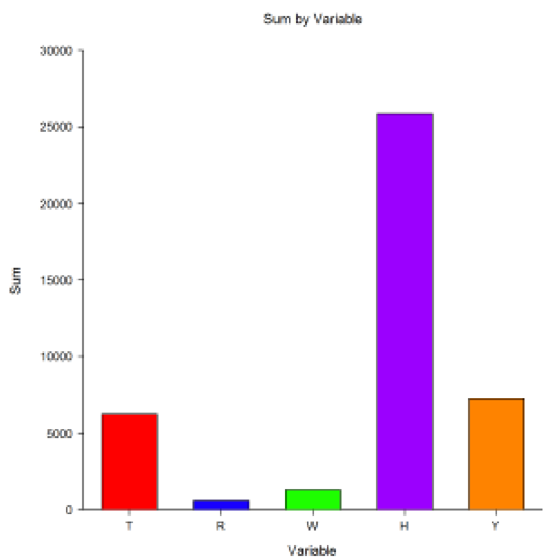

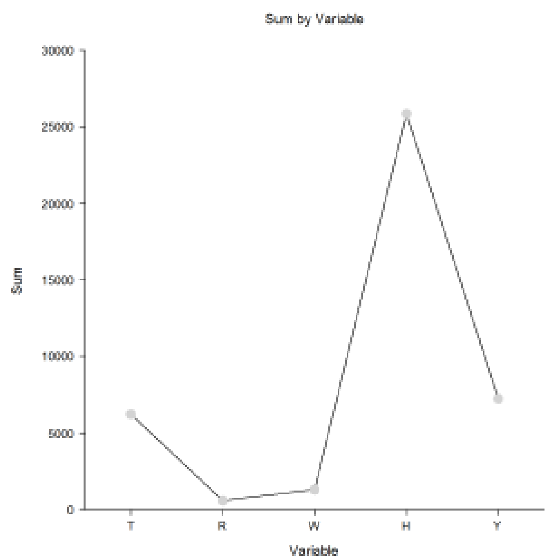

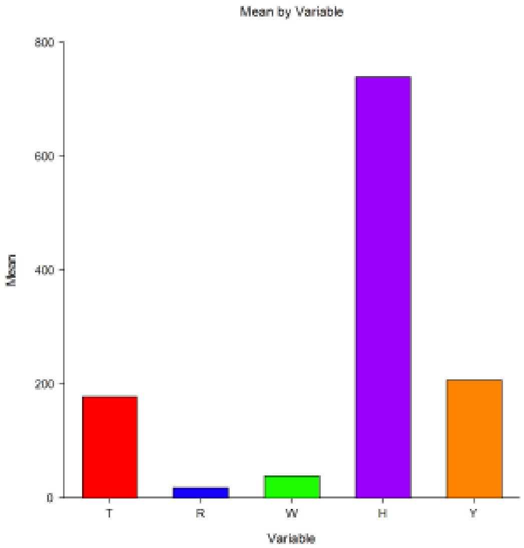
Mean by Variable
800
600
400
200
0
Mean
T
R
W
H
Y
Variable

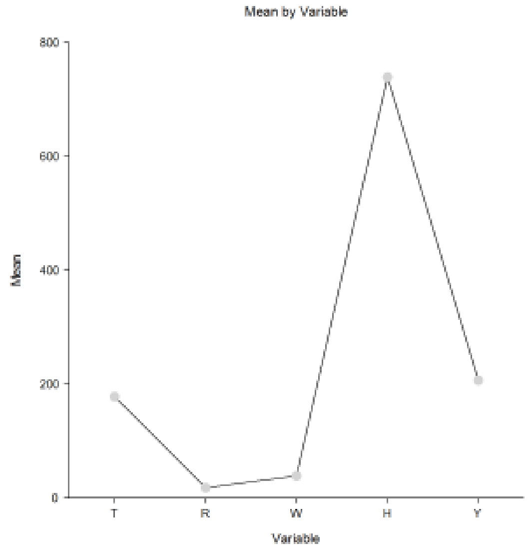
Mean by Variable
800
600
400
200
0
Mean
T
R
W
H
Y
Variable

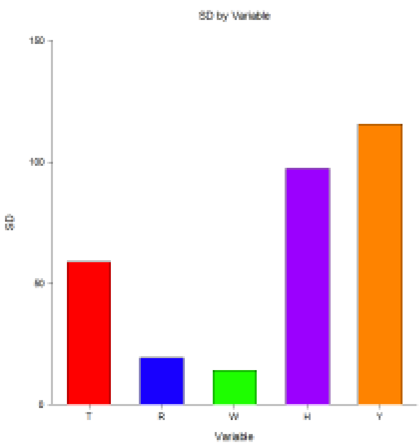
SD by Variable
SD
T
R
W
H
Y
Variable

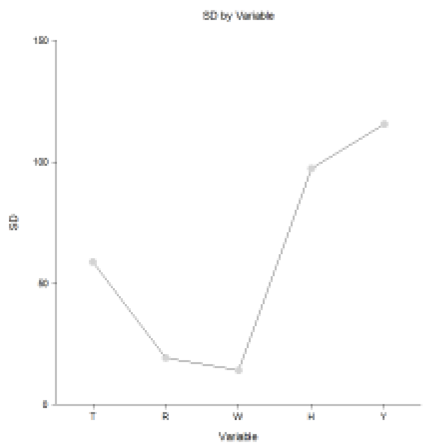
SD by Variable
SD
T
R
W
H
Y
Variable

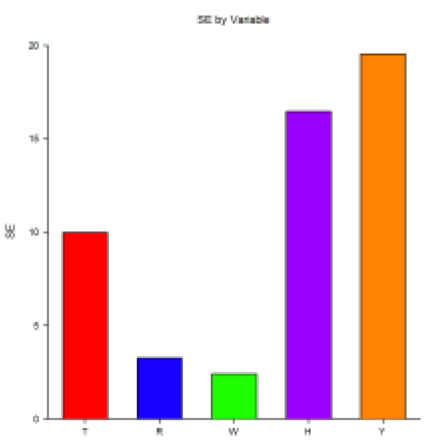
SE by Variable
20
15
10
5
0
SE
T
R
W
H
Y
Variable

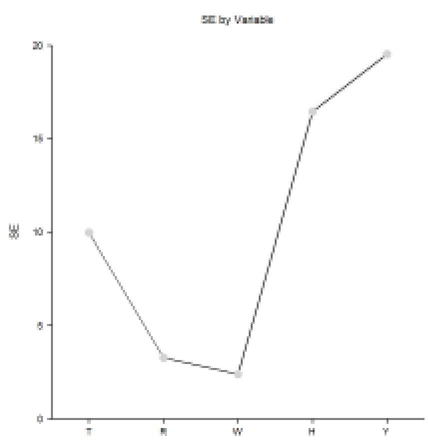
SE by Variable
20
15
10
5
0
SE
T
R
W
H
Y
Variable

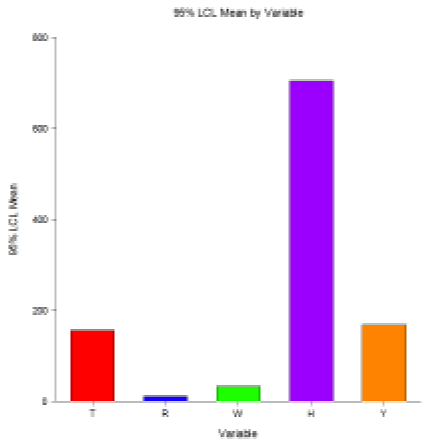
95% LCL Mean by Variable
95% LCL Mean
800
600
400
200
0
T
R
W
H
Y
Variable

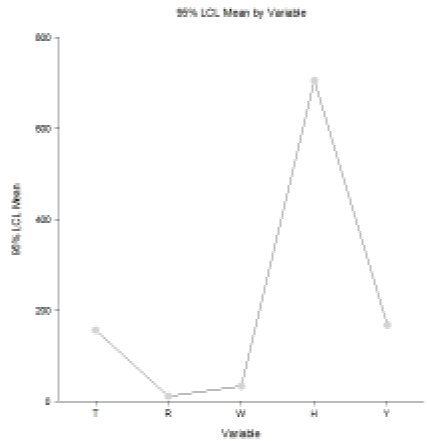
95% LCL Mean by Variable
95% LCL Mean
800
600
400
200
0
T
R
W
H
Y
Variable

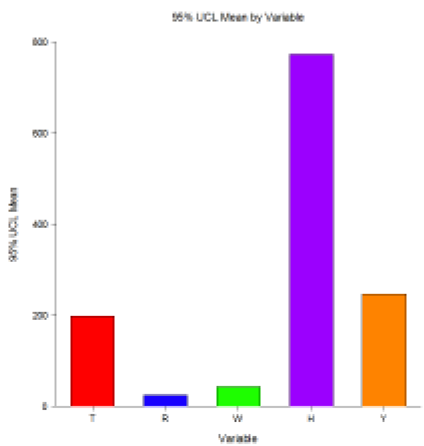
95% UCL Mean by Variable
800
600
400
200
0
T
R
W
H
Y
Variable

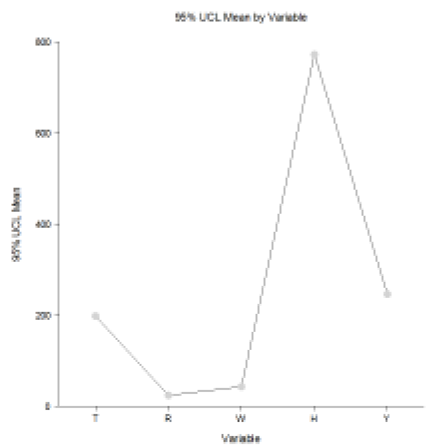
95% UCL Mean by Variable
800
600
400
200
0
T
R
W
H
Y
Variable

Dataset Untitled

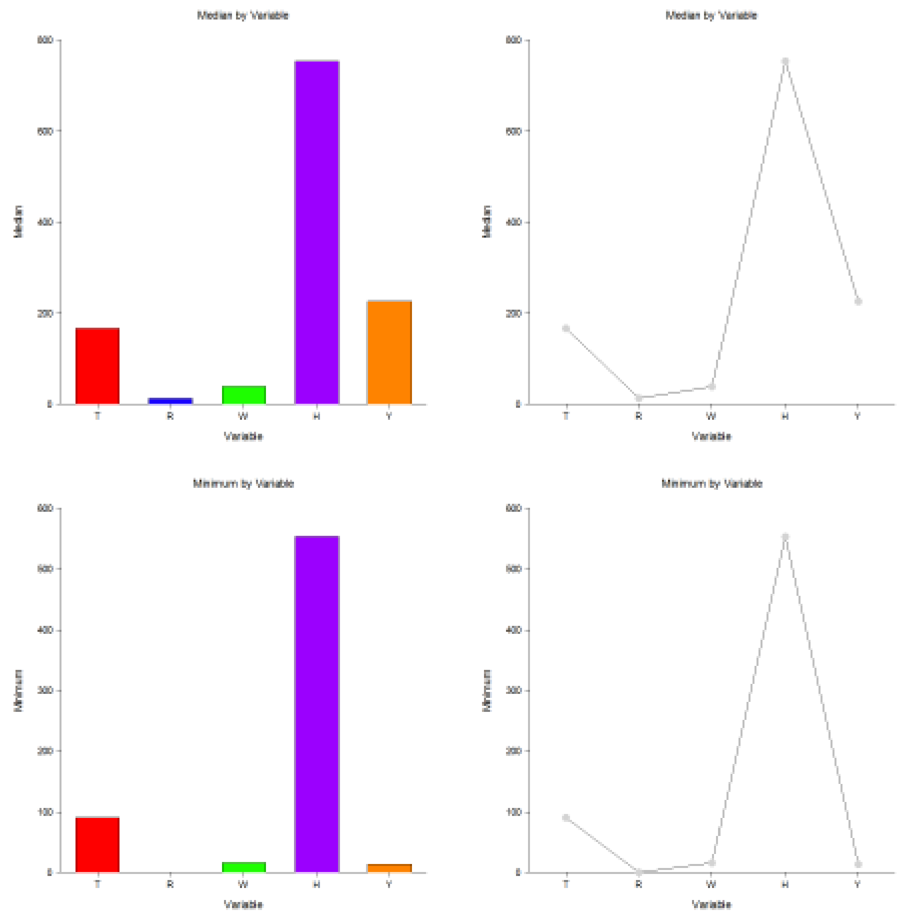

Dataset Untitled

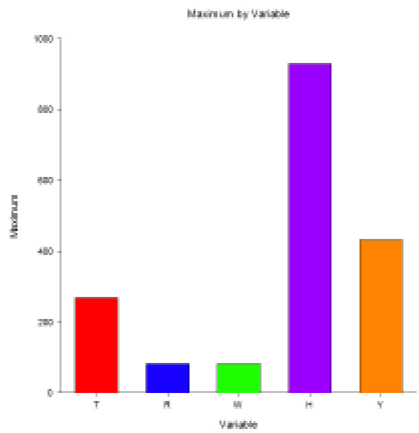

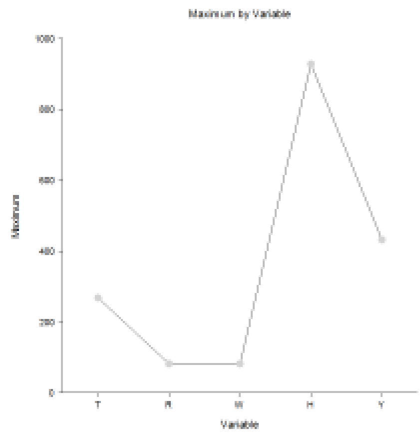

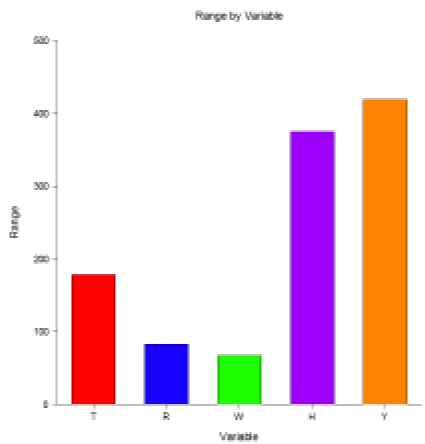

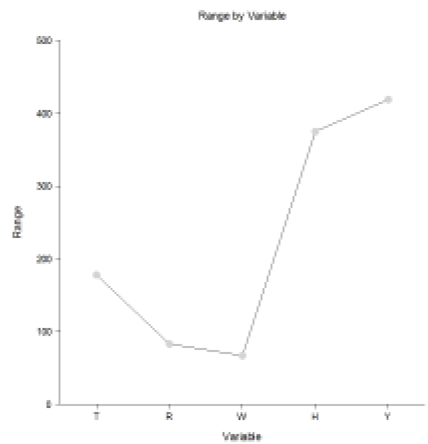

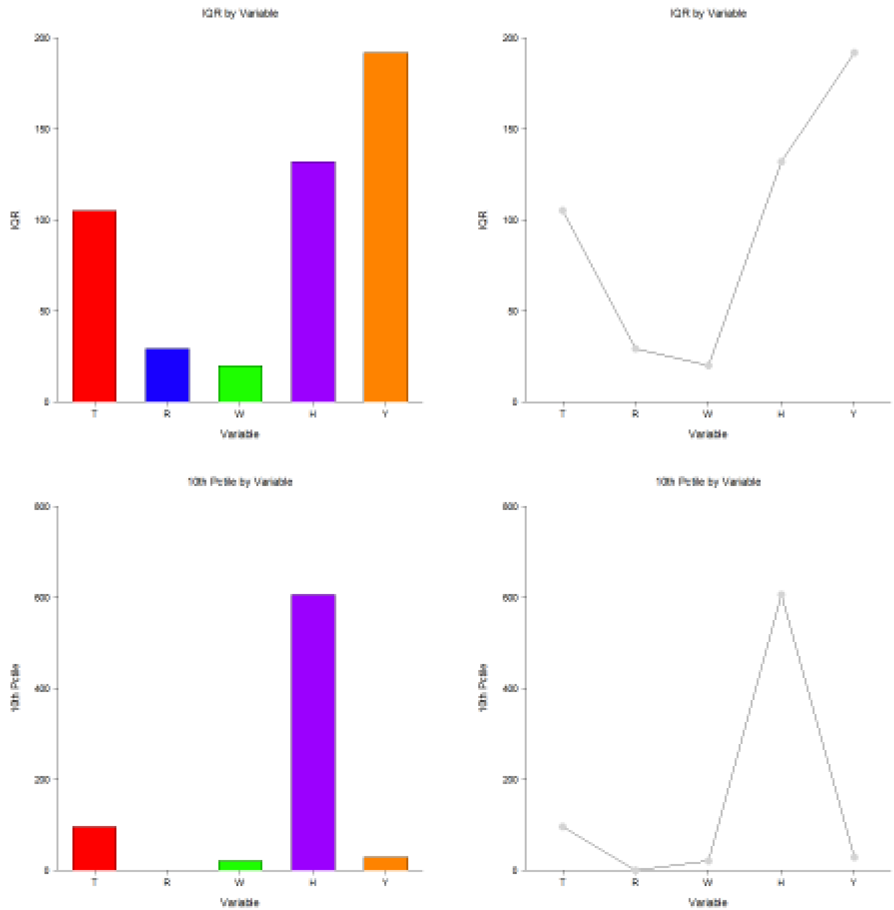
IQR by Variable
IQR
Variable
T
R
W
H
Y
0
50
100
150
200
IQR by Variable
IQR
Variable
10th Pctile by Variable
10th Pctile
Variable
0
200
400
600
800
10th Pctile by Variable
10th Pctile
Variable

Dataset   Untitled

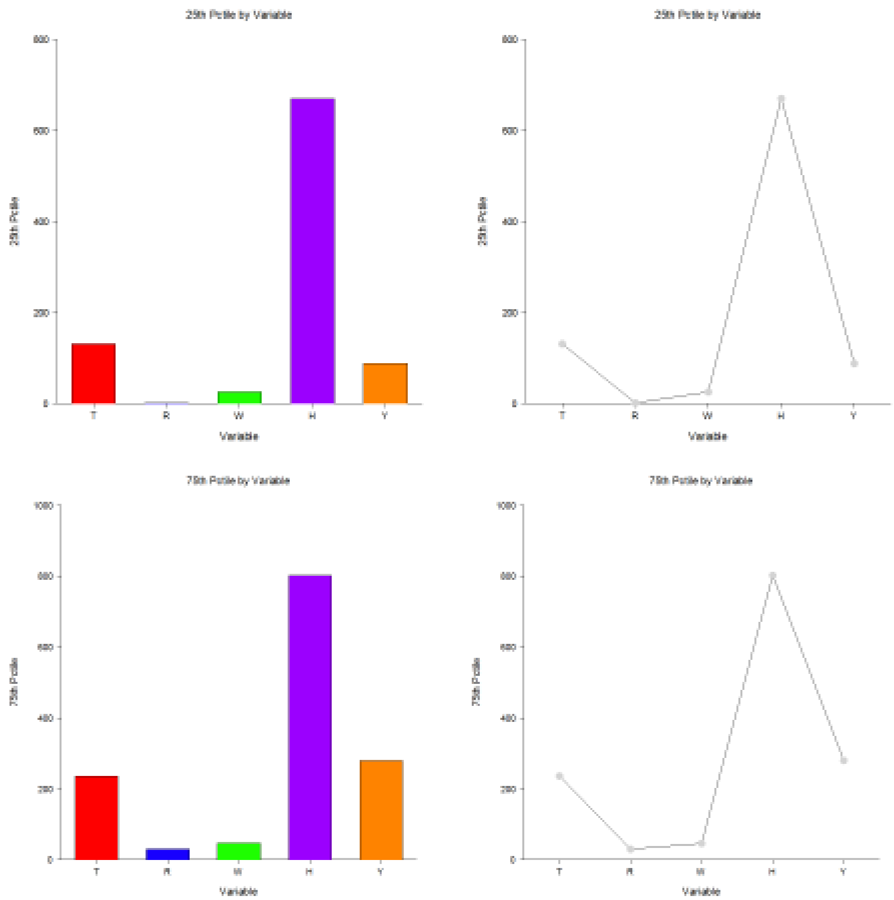

Dataset Untitled

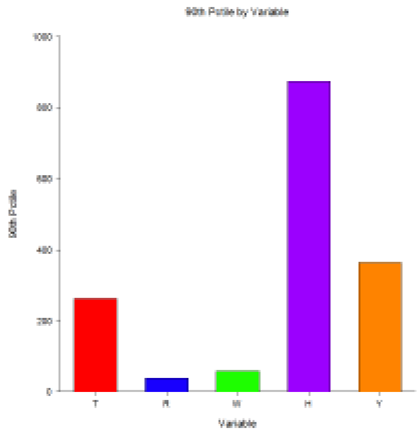

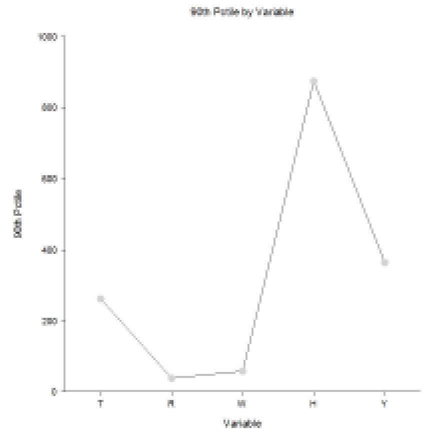

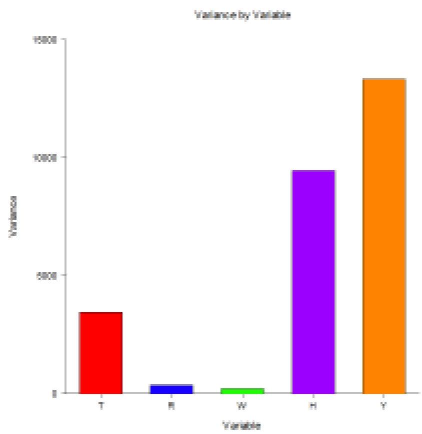

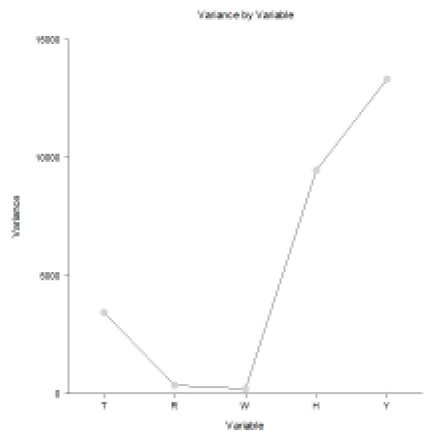

Dataset Untitled

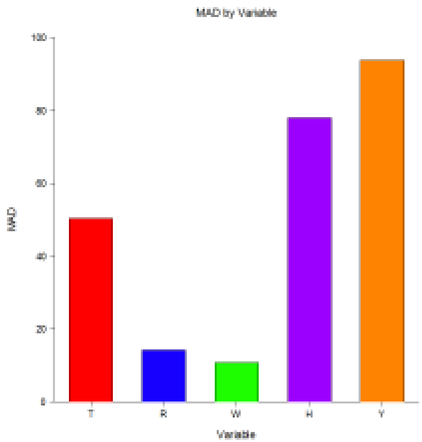

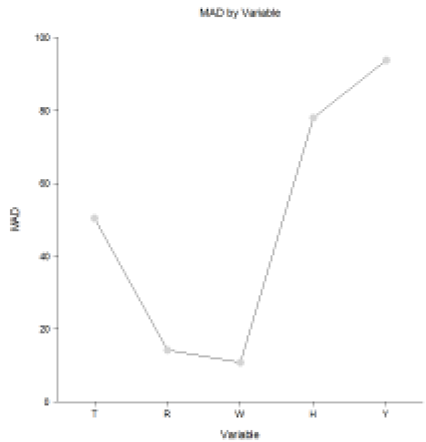

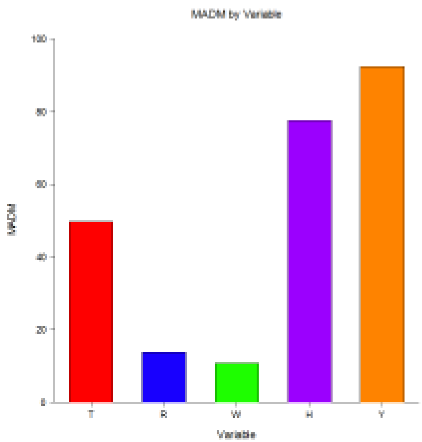

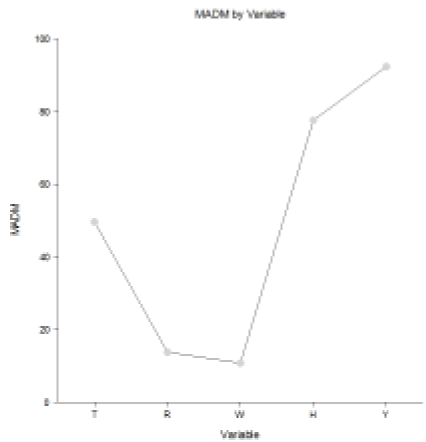

Dataset Untitled

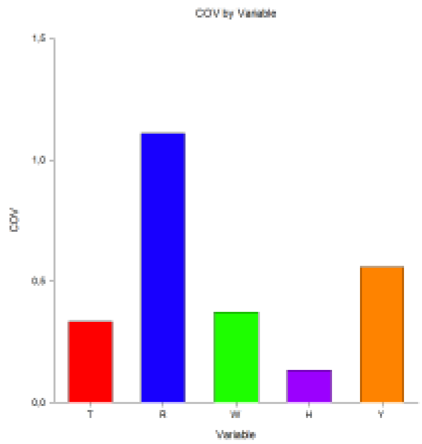

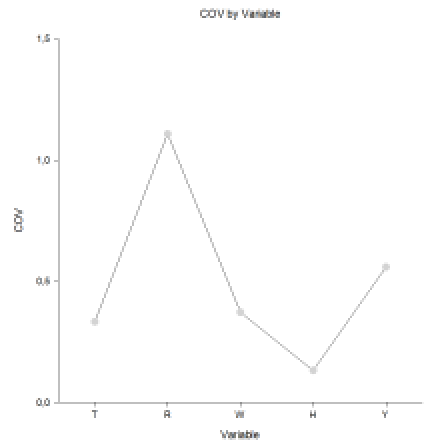

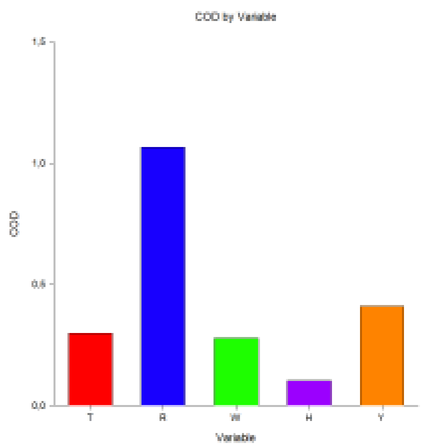

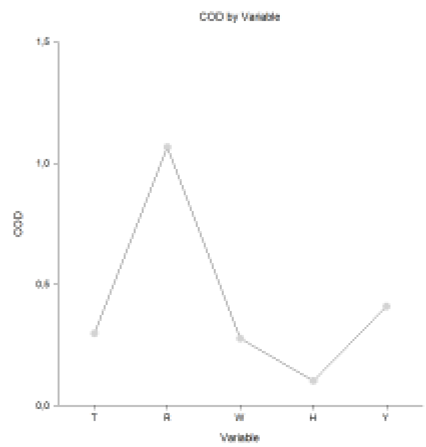

Dataset Untitled

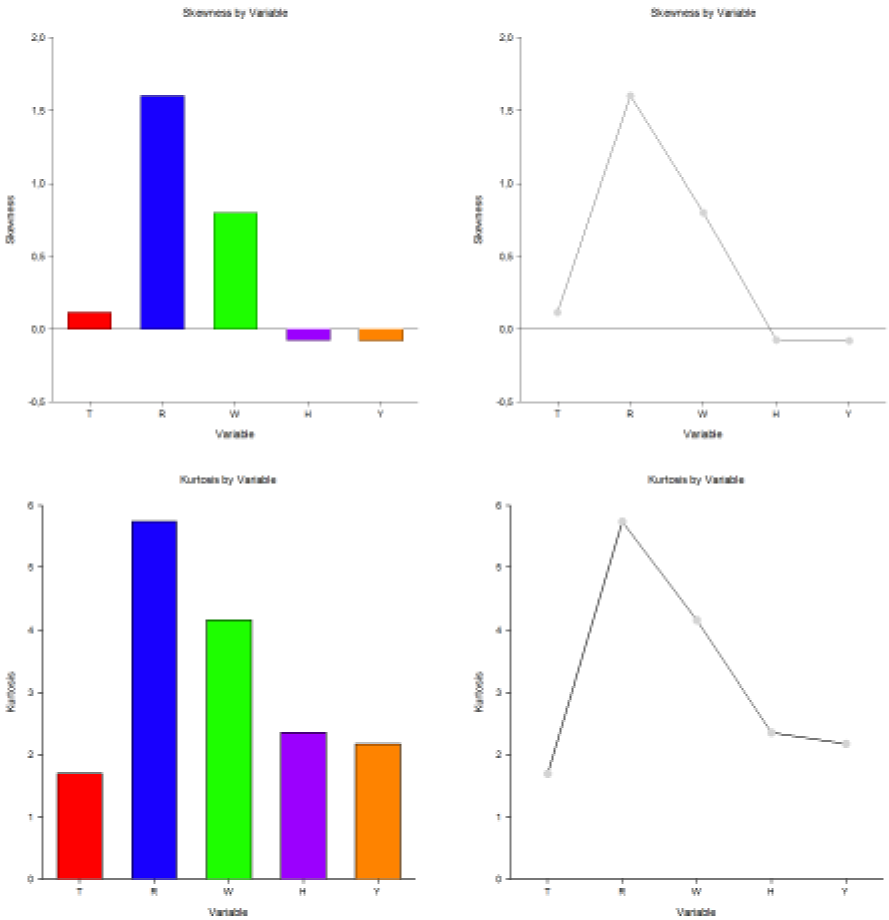

Conclusion

In this research I present statistical methods of GoNM system.

Acknowledgements

This work is co-financed by the Republic of Slovenia and the European Union from the European Regional Development Fund, by the Slovenian Research Agency (ARRS).

Reference

Babbie, Earl R. (2009). *The Practice of Social Research* (12th ed.). Wadsworth. pp. *436–440*. *ISBN 978-0-495-59841-1*.

Scientific error since 1785

Mihelič Janko, Domžale, Slovenija
mihelic.jani72@gmail.com

- Basic rule of trigonometry. Very old, nameless physical law. If we assume a field source, a point source of light with radius **r**, light strength decreases with distance.
- The same relation applies for electric and magnetic field strength. The rule explains that the field's strength weakens with distance and that it has the shape of the sphere.
- **We must read the equation from both sides!** The distance decreases depending on the field strength. The field determines the length measures and the velocities.
- Coulomb's (inverse square) law is fundamental physical law of electromagnetism, first published in 1785. This well known relation must be interpreted as „field dependent length contraction" when assuming that the sphere's radius **r**, as well as all other dimensions and velocities affected by a field are determined by it. In this way, all kinds of attractive forces, including gravity must be understood as field effects occurring when one body is located within another's field of influence and vice versa.

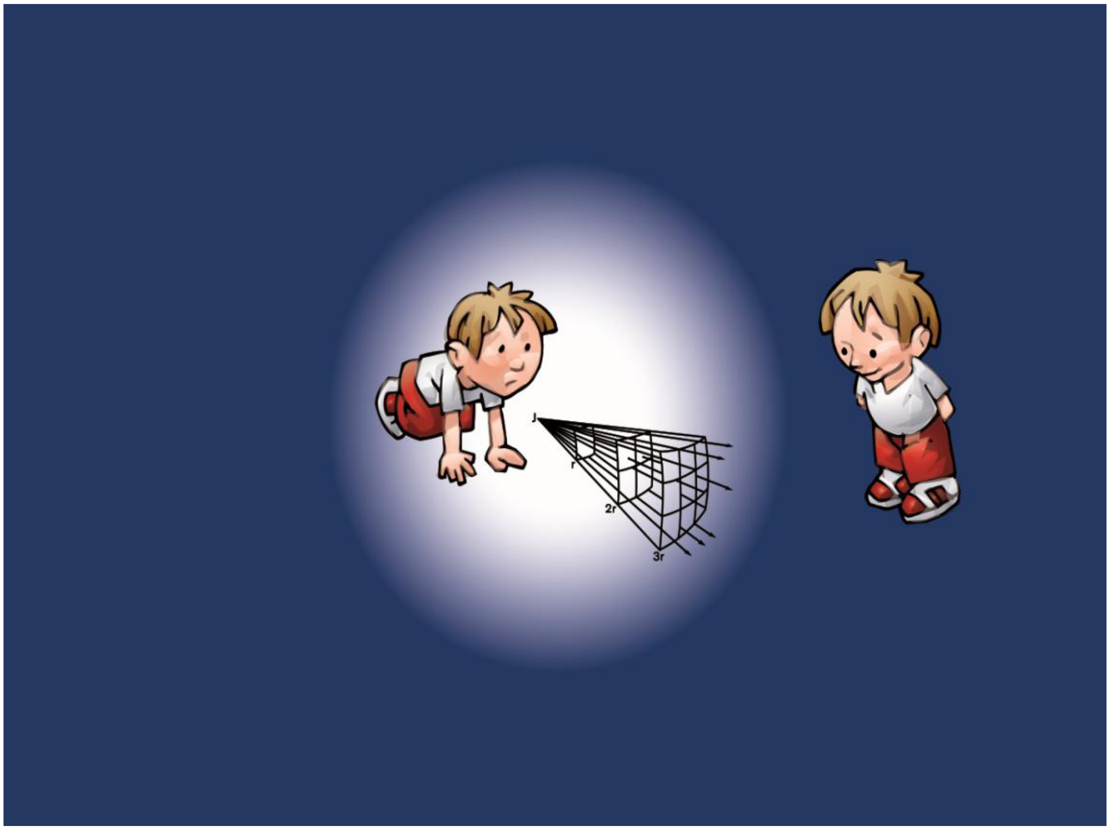

Goldfish problem

Problem of the inverse square law is the physical measurements that we observe within the system, but we cannot observe and measure them outside the system. The fish is in fishbowl, but it can't physically take a look at itself and take measurements from the outside on the inside. The energy sent by the transmitter to the receiver is expanded both during the signal transmission and during the bouncing return throughout the space (which means geometrically over the surface of the sphere), so the inverse square for both paths means that the transmitter will receive energy according to the inverse fourth power of range. Well, modern physics is a false theory.

Are we lawbreakers when we apply the gravitational force instead of the field in our environment, which is capable of doing the same thing?

The speed (m/s) also depends on the field strength and is therefore not fixed! We and our measuring devices cannot detect this as we are also in this field, our solar system. The speed of light is proportional to the measurement path. The result at all events is a constant value. **Speed of light is a constant of measurement and not a constant of nature.**

References:

Prof. Dr. Konstantin Meyl, author of Unified Field Theory: Potential vortex Vol. 5 page 13,14 Potential Vortex Vol.4 page 59,60.